

ABSTRACT

1
2
3
4
5
6
7
8
9
10
11
12
13
14
15
16
17
18
19
20
21

The vertical structure of Arctic low-level clouds and Arctic boundary layer is studied, using observations from ASCOS (Arctic Summer Cloud Ocean Study), in the central Arctic, in late summer 2008. Two general types of cloud structures are examined: the “neutrally-stratified” and “stably-stratified” clouds. Neutrally-stratified are mixed-phase clouds where radiative-cooling near cloud top produces turbulence that generates a cloud-driven mixed layer. When this layer mixes with the surface-generated turbulence, the cloud layer is coupled to the surface, whereas when such an interaction does not occur, it remains decoupled; the latter state is most frequently observed. The decoupled clouds are usually higher compared to the coupled; differences in thickness or cloud water properties between the two cases are however not found. The surface fluxes are also very similar for both states. The decoupled clouds exhibit a bimodal thermodynamic structure, depending on the depth of the sub-cloud mixed layer (SCML): clouds with shallower SCMLs are disconnected from the surface by weak inversions, whereas those that lay over a deeper SCML are associated with stronger inversions at the decoupling height. Neutrally-stratified clouds generally precipitate; the evaporation/sublimation of precipitation often enhances the decoupling state. Finally, stably-stratified clouds are usually lower, geometrically and optically thinner, non-precipitating liquid-water clouds, not containing enough liquid to drive efficient mixing through cloud-top cooling.

1 **1. Introduction**

2 Rapid changes in the Arctic climate during the past decades (Serreze et al., 2000;
3 Overland et al., 2004; ACIA 2005) have led to widespread attention in the global
4 climate research community. Annual average near-surface temperatures in the Arctic
5 have increased by over a factor of two compared to the rest of the world (ACIA
6 2005; Richter-Menge, 2010) and the sea-ice extent has been declining at an
7 accelerating rate, especially during summer and early fall (Comiso, 2002; Nghiem et
8 al., 2007; Stroeve et al., 2012). Extreme anomalies in the mid-September ice extent
9 minima over the last decade (Serreze et al., 2007; Stroeve et al., 2012), including
10 record minima in 2007 (Maslanik et al., 2007; Lindsay et al., 2009) and 2012
11 (Simmonds and Rudeva, 2012; Devasthale et al., 2013; Zhang et al., 2013) are
12 indicative of an increasing “Arctic amplification” (Serreze and Francis, 2006;
13 Serreze and Berry, 2011) signaling rapid climate change. This amplification has been
14 attributed to several factors that affect the surface energy budget; one is the surface-
15 albedo feedback (Perovich et al., 2008; Stroeve et al., 2012) and how changes at the
16 surface impact the cloud response (Kay and Gettelman, 2009), and vice versa. Other
17 amplification hypotheses exist, such as the lapse-rate feedback associated with the
18 vertical structure of warming (Bintanja et al., 2012; Pithan and Mauritsen, 2014), or
19 how changes in the large-scale northern hemisphere atmospheric circulation
20 (Graversen et al., 2008; Kapsch et al., 2013) may result in changes in the clouds and
21 hence the surface energy balance.

22 Global climate models exhibit a large variation in global and regional
23 sensitivity to imposed large-scale forcing, which has been attributed to differences in
24 cloud parameterization schemes and cloud feedbacks, especially those of low-level
25 clouds (Bony and Dufresne, 2005; Webb et al., 2006; Lauer et al., 2010). To
26 understand the Arctic climate system, a detailed understanding of cloud processes
27 and their impact on both the surface and atmospheric thermodynamic structure are
28 required (Curry et al., 1996). In general, solar radiation is reflected by clouds,
29 leading to a radiative cooling at the surface, whereas longwave radiation is both
30 absorbed and emitted by clouds. Over the Arctic, where surface albedo and solar
31 zenith angles are relatively large and clouds are predominantly low, the net effect on
32 the sea ice surface is a warming (Shupe and Intrieri, 2004; Sedlar et al., 2011),
33 except possibly for a short period in summer, when the surface albedo is reduced by

1 sea ice melt (Intrieri et al., 2002). The influence of the clouds on the surface energy
2 budget depends on several parameters, such as the cover, phase, and vertical and
3 horizontal cloud distribution, etc. (Randall et al., 1998); combining all the factors is
4 complex and it is no surprise that clouds are very difficult to model.

5 Low-level clouds are very frequent in the Arctic, especially during the summer
6 when they occur for 80-90% of the time (Curry and Ebert, 1992; Wang and Key,
7 2005; Tjernström, 2005; Shupe et al., 2011). Clouds below 3 km a.s.l (above surface
8 level; unless otherwise stated all heights will be given above the surface) over the
9 Arctic are most frequently mixed-phase, consisting of both droplets and ice crystals
10 (Shupe, 2011); the liquid is often concentrated in a relatively thin layer near the top
11 of the cloud, with near-continuous precipitation consisting of frozen drizzle or ice
12 crystals formed within the liquid layer (Shupe et al., 2008). These clouds have been
13 observed to persist for long durations – hours to days (Shupe et al., 2011) – and are
14 believed to have a critical impact on the surface energy balance (Intrieri et al., 2002;
15 Persson et al., 2002; Shupe and Intrieri, 2004; Sedlar et al., 2011). Both short- and
16 longwave radiation are very sensitive to cloud phase; longwave opacity (emissivity)
17 increases asymptotically to unity with cloud liquid water path, while shortwave
18 reflection to space increases with increasing numbers of smaller, spherical cloud
19 droplets (e.g., Twomey, 1977; Stephens, 1978). The end result is more longwave
20 radiation emitted to the surface and less shortwave radiation transmitted to the
21 surface when liquid droplets are present than for ice-only clouds (Shupe and Intrieri,
22 2004; Prenni et al., 2007).

23 Mixed-phase clouds are particularly poorly handled by current climate models
24 (Tjernström et al., 2005; 2008; Karlsson and Svensson, 2010), suggesting that the
25 processes that support the maintenance of these clouds in the Arctic are not fully
26 understood. These processes are discussed in Morrison et al. (2012). For example,
27 turbulence generated by cloud-top cooling and in-cloud upward air motion play a
28 critical role; the layer with largest liquid concentrations near cloud top emits
29 longwave radiation to space (Pinto, 1998), which decreases static stability in the
30 clouds and leads to a buoyant overturning circulation (e.g., Nicholls, 1984). These
31 cloud-driven turbulent motions promote the growth of both liquid and ice, rather than
32 just ice growing at the expense of the liquid (Korolev, 2007) as would intuitively be
33 expected in an ice/liquid mixture. Moreover, mixing from below cloud base may also

1 be ongoing, driven by surface forcing and/or advection in the lower troposphere,
2 leading to an upward transfer of heat and moisture. The coupling, or lack thereof
3 (hence referred to as decoupling), between cloud- and surface-generated turbulence
4 may be critically important for the sustenance of mixed-phase clouds.

5 Because of the strongly stable near-surface conditions that often occur during
6 Arctic winter to early spring (Kahl, 1992; Curry, 1986), surface fluxes are often
7 considered to have no significant contribution to the cloud's moisture during these
8 seasons; this changes from late spring until October when both open ice-free ocean
9 and melting sea ice expose a vast source of heat and moisture to the relatively cool
10 and dry lower atmosphere (Pinto and Curry, 1995). Analysis of the vertical
11 atmospheric structure in late summer from four different expeditions, including the
12 Arctic Summer Cloud Ocean Study (ASCOS; www.ascos.se, also see Tjernström et
13 al., 2014) revealed a neutrally-stratified layer extending from the surface up to about
14 300-600 m (Tjernström et al. 2012), which indicates that the surface and the
15 boundary-layer clouds could potentially be thermodynamically coupled.

16 Shupe et al. (2013) investigated the interactions between the cloud and
17 boundary layer using one week of observations from ASCOS and found, however,
18 that for this time period, such coupling took place only 25% of the time; the rest of
19 the time the cloud layer was decoupled from the surface. In addition, even when
20 clouds were coupled with the surface, surface fluxes did not seem to drive this
21 coupling; instead they simply responded to the mixed-layer processes aloft, driven
22 primarily by in-cloud generated turbulence.

23 The present study is also based on ASCOS data and provides a complementary
24 view on cloud-surface interactions to that by Shupe et al. (2013); they analyzed three
25 case studies, each 9 to 12 hours long, to provide a process-level view of what
26 happens in these clouds; the time evolution and the transitions between coupled and
27 decoupled states were important aspects of this study. They also provided a statistical
28 description of some characteristics of the coupling states, although for a limited time
29 period and based only on single-cloud layer profiles. The present study offers a
30 complete statistical analysis on cloud-surface coupling and the main purpose here is
31 to identify properties in the thermodynamic structure that generally characterize the
32 state of cloud-surface coupling and assess which factors drive these interactions. The
33 connection between (de)coupling and precipitation structure is also investigated.

1 Moreover, while in Shupe et al. (2013) only clouds that generate turbulence are
2 examined, here we also identify clouds where the in-cloud mixing is inhibited; an
3 attempt to explain why the generation of cloud-driven motions is prevented in these
4 cases is also provided.

5 Apart from considering a different approach of the surface-cloud coupling
6 issue, the two studies also differ in method. Shupe et al (2013) used profiles of
7 turbulence dissipation rate, derived from Doppler radar velocities, to determine the
8 coupling state and the depth of the cloud-driven mixed layer below cloud base. Here
9 we instead use vertical profiles of equivalent potential temperature, $\Theta_E = \Theta (1 + L$
10 $Q_v / C_p T)$, a conserved quantity during moist adiabatic processes, to identify stability
11 and stability changes within the cloud and sub-cloud layers. While deriving profiles
12 of turbulence dissipation rate from the cloud radar requires more ideal conditions
13 (e.g. active mixing) than observing the thermal structure of the lowest troposphere,
14 our method allows us to examine profiles from all periods (Tjernström et al., 2012,
15 2013) of ASCOS, from the whole ice drift as well as the transit periods (to/from the
16 ice-drift). This allowed us to include substantially more data in our analysis with a
17 larger variety of meteorological conditions, compared to only the week-long period
18 characterized by relatively steady conditions and free-atmosphere subsidence.
19 Moreover, the dissipation rate method does not allow examination of decoupling
20 below 150 m (near the first radar vertical range gate), whereas profiles of Θ_E can
21 indicate decoupling much closer to the surface.

22 The present study is organized as follows; Section 2 includes a brief
23 description of ASCOS, the atmospheric conditions and the instrumentation deployed;
24 included here is also a discussion on the analysis methods. Section 3 describes the
25 results of this study, first examining the characteristics of surface turbulence and
26 cloud properties and then examining how the boundary layer responds to these
27 interactions - or the lack of. A discussion and the conclusions are given in Section 4
28 and 5, respectively.

1 **2. Data and methods**

2 **2.1 ASCOS**

3 ASCOS operated under the fourth International Polar Year (IPY 2007-2009) and was
4 an intensive field experiment observing many aspects of the atmosphere, sea ice and
5 the upper ocean for 40 days through August and late September 2008, in the North
6 Atlantic sector of the central Arctic Ocean (~87.2 N). Tjernström et al. (2014)
7 provides a detailed description of this endeavor, as well as of the instruments and
8 measurement strategies that were deployed. ASCOS was conducted on the Swedish
9 ice-breaker *Oden*, which left Longyearbyen on Svalbard on 2 August (Day of Year;
10 DoY 215) and returned on 9 September (DoY 253). Between 12 August (DoY 225)
11 and 2 September (DoY 246), *Oden* was moored to and drifted with a 3x6 km ice-
12 floe, where an ice camp was established. The drift track was approximately from
13 87°21'N and 01°29'W to 87°09'N and 11°01'W; this period will be referred to as
14 the “ice drift”. Note that the term “ice drift” is used here for the period when the
15 icebreaker was moored to and drifted with the ice; however, the whole dataset used
16 in this study, including the transitions, comes from within the ice pack. Ice cover
17 conditions were fairly similar throughout ASCOS, although the surface melt ended
18 and the freeze up started towards the end (Sedlar et al., 2011; Sirevaag et al., 2011)

19 Detailed observations of Arctic clouds are sparse, limited in time and space to
20 a small number of intensive observational campaigns, including SHEBA (Uttal et al.,
21 2002) and AOE-2001 (Leck et al., 2004; Tjernström et al., 2004) or the pan-Arctic
22 observatories discussed in Shupe et al. (2011). One aim of ASCOS was to study the
23 formation and life-cycle of low-level clouds, with a focus to better understand their
24 impact on the surface energy budget, especially during the fall transition towards
25 sea-ice freeze up. ASCOS included arguably the most comprehensive suite of
26 instruments for observing surface, atmospheric and cloud processes over a remote
27 sea-ice environment (Tjernström et al., 2014).

28 Large-scale atmospheric conditions during ASCOS are documented in
29 Tjernström et al. (2012) while detailed descriptions of the meteorological conditions
30 encountered during ASCOS ice drift are provided by Sedlar et al. (2011) and
31 Tjernström et al. (2012; 2013); hence only a brief recap will be provided here. Sedlar
32 et al. (2011) analyzed the surface energy budget during the ice drift and defined four

1 periods with different energy budgets and cloud characteristics. Tjernström et al.
2 (2012) included surface temperature variability and vertical structure of the lower
3 troposphere and subsequently divided the first period into two sub-periods, defining
4 five periods in total. These are the periods adopted here and Fig. 1 illustrates these 5
5 ice drift periods overlaid on the reflectivity from the vertically pointing cloud radar.
6 DoYs prior to 226 and after 246 are during the transit towards and away from the ice
7 drift, respectively.

8 The first (DoY 226-230) and second (DoY 230-234) periods during the ice
9 drift had the largest positive surface energy residuals, indicating melt was still
10 ongoing (Sedlar et al., 2011). Surface temperatures were primarily close to the
11 melting point of fresh water during these periods. Both periods were affected by
12 synoptic weather systems and deep frontal cloud structures, but the first was
13 synoptically more active and significantly more variable in temperature than the
14 second (Fig. 1). This period of synoptic activity ended on the evening of DoY 233.
15 During the third period (DoY 234-236) a sharp drop in temperature was observed,
16 down to -6 °C. Quiescent conditions prevailed during these two days and an
17 intermittent, and occasionally tenuous, low-level stratiform cloud or fog layer
18 emerged below an upper level, optically thin cirrus layer (Sedlar et al., 2011).

19 On DoY 236, a frontal system produced heavy snow fall during much of the
20 evening. After that, the following 4th period (DoY 236-244) was characterized by
21 high pressure and large-scale subsidence in the free troposphere, with only weak
22 frontal passages. Single and multi-layered stratiform clouds below 2 km were
23 persistent for nearly the entire week (Sedlar et al., 2011), topped by thin liquid cloud
24 layers with ice crystals growing within, and falling from, these layers. The surface
25 temperature was somewhat higher, close to the freezing point of ocean water, but
26 still below fresh-water melting. Sedlar et al. (2011) concluded that this period was
27 vital to the transition of the surface towards the seasonal freeze up. These relatively
28 steady conditions continued during the 5th period (DoY 244-246), when an area with
29 partly clear skies and optically thin clouds advected over the ASCOS site, allowing
30 surface temperatures to plummet below -12 °C and the autumn freeze up to initiate
31 (Sedlar et al., 2011). Finally, during both transit periods, before and after the ice
32 drift, numerous synoptic weather systems were encountered; see Tjernström et al.
33 (2012) for detailed profiles of radar reflectivity and subjective analysis of frontal

1 profiles during each of these periods.

2

3 **2.2 Instrumentation**

4 A detailed description of all ASCOS instrumentation is provided by Tjernström et al.
5 (2014). Here, only basic information about the instruments used in this study is
6 given, while further details can be found in the cited references.

7 Information on the vertical atmospheric structure is derived from radiosondes
8 and a 60-GHz scanning radiometer. Radiosoundings were released approximately
9 every 6 hours. Although the limited temporal resolution is a major disadvantage,
10 radiosondes provide accurate temperature, moisture and wind measurements. The
11 scanning radiometer (Westwater et al., 1999) provides temperature profiles up to
12 1200 m with a vertical resolution of around 7 m near the surface, gradually
13 deteriorating with altitude to about 200 m at 1 km. A 5-min averaging window was
14 applied to the 1-Hz raw data to improve the signal-to-noise ratio. The scanning
15 radiometer has been shown to provide accurate measurements, with a low root mean
16 square error relative to independent radiosondes up to 800 m (P.O.G. Persson,
17 personal communication, 2013); above this height, the scanning radiometer
18 temperatures gradually revert to the linear interpolation between the radiosonde
19 profiles used as the a priori assumption in the retrieval process. Nevertheless, due to
20 its high temporal resolution, and the fact that many of the cloud and sub-cloud layers
21 are below 800 m, these profiles provide a valuable coherent data set of temperature
22 profiles.

23 Cloud boundaries and characteristics are, to a large extent, derived from a
24 vertically-pointing 35-GHz Doppler Millimeter Cloud Radar (MMCR; Moran et al.,
25 1998). The vertical resolution is 45 m with a lowest radar gate at 105 m and a time
26 resolution of 10 s. The measured Doppler spectrum was processed to estimate the
27 three Doppler radar moments: radar reflectivity (dBZ), mean Doppler velocity (m s^{-1})
28 and Doppler spectrum width (m s^{-1}) in clouds and precipitation. The reflectivity,
29 which is nominally proportional to hydrometeor size to the sixth power, is usually
30 dominated by ice crystals since they are normally larger than liquid droplets. The fall
31 velocity of the hydrometeors can also be used to assist in distinguishing hydrometeor
32 phase; cloud droplets have a very small, nearly negligible, fall velocity, whereas ice

1 crystals and drizzle/rain droplets generally fall with larger velocities. As is common
2 in radar meteorology, a positive Doppler velocity is defined downward. The Doppler
3 spectrum width can provide indications of multiple cloud phases, i.e., particles in the
4 same volume with different fall speeds, and/or turbulence within the radar pulse
5 volume.

6 Under most observed conditions, the MMCR can accurately identify cloud top;
7 however when precipitation occurs between multi-layer clouds, the MMCR may not
8 provide information on cloud top height for lower layers. The full Doppler spectra
9 were used to create spectrographs of vertically-resolved reflected power as a function
10 of Doppler velocity. These proved useful for distinguishing multiple cloud layers
11 when other sensors indicated the potential for cloud layering masked by
12 precipitation; spectrographs are discussed in Section 2.3.

13 MMCR derived cloud boundaries are also complemented with additional
14 remote sensors. Cloud base is derived using two laser ceilometers with a sampling
15 interval of 15 s. In general, laser ceilometers become attenuated by large
16 concentrations of liquid droplets; this instrument is therefore able to penetrate
17 precipitating layers of ice crystals and drizzle droplets and identify the vertical
18 locations of up to 3 cloud bases, provided the lower cloud layers are not too optically
19 thick. Once the return signal is attenuated, it is not possible to detect additional cloud
20 layers aloft. A comparison of the two time series revealed relatively good agreement
21 between the two ceilometers.

22 A dual-channel microwave radiometer provides vertically-integrated liquid
23 water path (LWP) retrievals with an uncertainty of 25 g m^{-2} (Westwater et al., 2001);
24 ice water path (IWP) is estimated using a multi-sensor cloud phase classification and
25 MMCR reflectivity power-law relationship (Shupe et al., 2005). Cloud condensation
26 nuclei (CCN) concentration was measured by an *in situ* CCN counter (Roberts and
27 Nenes, 2005), set at a constant supersaturation of 0.2%, based on typical values used
28 in other similar expeditions (Bigg and Leck, 2001; Leck et al., 2002). These CCN
29 measurements were made on the ship via an inlet at 25 m above the surface.

30 Finally, turbulent fluxes are derived using two techniques. Eddy covariance
31 measurements are available from the ice drift (12 August – 1 September) at heights
32 between the surface and 30 meters from sensors deployed on masts on the ice. The

1 uncertainty of individual turbulent flux estimates is not easy to determine but is
2 generally considered to be around 10% (Andreas et al., 2005). Diffusional and rime
3 icing on the turbulent flux instrumentation poses a more critical problem, and leads to
4 time periods when turbulent fluxes could not be estimated. To maximize the use of
5 this data, a single consensus time series was created from all available data, regardless
6 of height, assuming it was all sampled within the so-called "constant-flux layer"; tests
7 indicate that this is a reasonable approximation.

8 So-called “bulk turbulent fluxes”, based on mean vertical differences, are less
9 accurate than direct measurements but data from instruments onboard the ship allow
10 fluxes to be estimated for the whole expedition. Static stability is estimated from the
11 Marine Atmospheric Emitted Radiance Interferometer (MAERI) instrument onboard
12 *Oden* to fill missing data periods from the eddy correlation measurements, as well as
13 to extend the observations of turbulent fluxes to the entire ASCOS expedition. The
14 MAERI measured air temperature, viewing horizontally out from its position at 21 m
15 on the port side of the ship, and the surface temperature, viewing down at the surface
16 from the same position; since the same sensor is used for both, the temperature
17 difference is not affected by systematic errors. These data were combined with the
18 observed humidity, assuming a saturated surface with respect to the observed
19 temperature, and wind speed from the ship’s weather station to obtain the turbulent
20 fluxes using the TOGA COARE bulk flux scheme, modified for Arctic sea-ice
21 conditions (Persson et al., 2002). However, MAERI temperatures were sometimes
22 affected by certain physical factors; when the ship was oriented so that the MAERI
23 sensor viewed open ocean, rather than ice, it sometimes measured a higher
24 temperature than over the adjacent ice surface, leading to an overestimation of the
25 heat fluxes. Also, when the wind direction was from *Oden*’s starboard side, across
26 the ship, the MAERI, being located on the port side, may have observed too high air
27 temperatures due to the heat plume from the ship; then the sensible heat flux is likely
28 underestimated.

29

30 **2.3 Analysis method**

31 The first MMCR range gate in the vertical with a return power below the radar
32 sensitivity demarcates the cloud top, while the highest observed ceilometer cloud

1 base below cloud top is considered as the base for this layer. Both ceilometers are
2 used for consensus. Median cloud boundaries were computed from a 2-min window
3 following each scanning radiometer measurement and a 10-min window following
4 each radiosonde release. For the analysis of cloud bulk properties (LWP, IWP) and
5 the radar Doppler moments, the same time windows were used to derive median
6 values. Considering the persistence of low-level Arctic clouds (Shupe et al., 2011),
7 the assumption that the median cloud layers are in steady state over the above
8 applied time-windows is reasonable. Median boundaries are used, instead of the
9 mean, in order to reduce the effect of outliers (Sedlar et al., 2011), as may
10 occasionally occur with only slightly less than complete overcast conditions, or when
11 a second cloud layer emerges within the time window following thermodynamic
12 profiles.

13 Profiles of Θ_E are used to define the cloud-driven turbulent mixed layer;
14 depending on whether this layer extends down to the surface or not, the cloud is
15 classified as either “coupled” or “decoupled”, respectively. If a cloud-driven mixed
16 layer is not observed, then the cloud is classified as “stably-stratified”. Note that
17 “stably-stratified” clouds are also not connected to the surface; here the word
18 “decoupled” refers only to cases with a cloud-driven mixed layer. Two sets of data
19 are used; either using the radiosoundings directly or combining the higher frequency
20 scanning radiometer temperature profiles with interpolated specific humidity from
21 the soundings. While the radiosonde equivalent potential temperature data is more
22 accurate, it has temporal limitations. On the other hand, while the interpolation of
23 specific humidity is a limitation for the scanning radiometer data, it allows using a
24 higher temporal resolution and increases the number of profiles included in the
25 study. The classification of vertical thermodynamic structure of the clouds based on
26 the scanning radiometer profiles is in good agreement with the results derived from
27 the radiosonde dataset. Therefore, the majority of the results in this study are based
28 on the scanning radiometer, while for other information the radiosonde data is used
29 (e.g., humidity and wind).

30 An algorithm was developed to identify the main temperature inversion in the
31 layer extending above cloud base until 100 m above cloud top, by applying
32 thresholds to the Θ_E profiles. A quasi-constant Θ_E from the inversion base down to
33 the surface is taken to indicate coupling, whereas a decrease towards the surface

1 below the cloud indicates a local stable layer and hence decoupling. The height at
2 which the Θ_E has decreased by 0.5°C , compared to the cumulative mean value of the
3 layer above, is considered to be the decoupling height. This threshold was selected to
4 optimize between accuracy and reliability, given the vertical variability of the
5 observed temperature, especially in the soundings, and the results were reasonably
6 insensitive to small changes in the threshold. The layer between the cloud base and
7 the decoupling height will be referred as the sub-cloud mixed layer (SCML). Both
8 coupled and decoupled clouds will be often referred as neutrally-stratified clouds,
9 referring to the gradient Θ_E profile within the cloud layer. If the gradient of Θ_E is
10 positive through the whole cloud layer, it is classified as a stably-stratified or stable
11 cloud. Moreover, profiles with no inversion near cloud top were reexamined by
12 estimating the Θ_E gradient from cloud top to cloud base. These profiles were found
13 to have large gradients and so these cases are also considered to be stable clouds. To
14 illustrate qualitatively the differentiation of the categories using the Θ_E profiles,
15 examples are given in Fig. 2 for coupled (Fig. 2a), decoupled (Fig. 2b) and stable
16 clouds with a main inversion identified close to the cloud top (Fig. 2c) and with no
17 main inversion identified (Fig. 2d).

18 Only profiles with a cloud top below 1500 m, a cloud base below 1200 m and a
19 cloud thickness larger than 135 m (three radar gates) are included in the analysis. It
20 is not possible to evaluate how these choices affect the results, since these limits are
21 set by real limitations in the instruments that cannot be freely varied. In addition,
22 profiles where cloud thickness is greater than 700 m are assumed to be two cloud
23 layers with precipitation falling from the upper cloud and where the ceilometer fails
24 to penetrate the lower cloud to detect the upper cloud base; the choice of this
25 threshold is based on relative results by Shupe et al. (2013), who included only
26 single cloud layers in their analysis. For some of these cases, it is possible to
27 estimate the upper cloud base from spectrographs. Two examples are shown in Fig.
28 3. For these cases, the cloud top detected by the MMCR is the top of the upper cloud,
29 whereas the existence of a lower dense cloud prevents the ceilometer from
30 measuring the corresponding upper cloud base height. In the cases in Fig. 3, the
31 cloud top and base derived directly from the instruments is 960 m and 90 m, and
32 1095 m and 75 m, respectively, but from the spectrographs we could infer that there
33 are two cloud layers present and the base of the upper clouds are around 750 m and

1 700 m, respectively. These are identified as the levels where the Doppler velocities
2 become systematically large and positive, indicating only falling hydrometeors and
3 an absence of liquid cloud droplets, assuming that the latter are small and have
4 negligible (near 0 m s^{-1}) fall velocities. Hence the height where significant radar
5 power crosses the zero velocity line is indicative of the liquid base height.

6 Using radiosonde profiles for the classification, the same cloud thickness
7 criteria are applied, since they are due to the MMCR, but a less strict cloud top
8 criterion is applied, including cloud returns up to 3000 m. The less strict cloud-top
9 criterion for the radiosonde profiles allows more cases to be included and is
10 consistent with the aim to analyze stratocumulus. It is chosen because of the shorter
11 time-series that this instrument provides and the need to include as many profiles as
12 possible in our analysis.

13 Applying the above criteria, 3436 out of the total available 8261 scanning
14 radiometer profiles are considered, or 42% data coverage. For almost 40% of the
15 available ASCOS profiles, a proper low cloud top, as defined above, was not
16 detected by the radar due to the presence of deep precipitating weather systems (see
17 Fig. 1), whereas around 18% fail to pass the geometrical restrictions. Hence,
18 considering only the times when deep weather systems were not present, the
19 algorithms described above captures roughly two thirds of the available data. As a
20 comparison, 87 out of the 145 (~60%) radiosonde profiles pass the above criteria for
21 similar reasons.

22 To investigate the liquid and ice water cloud properties that characterize each
23 cloud state, single cloud-layer profiles had to be selected, since the derived LWP is a
24 vertically-integrated quantity; the vertical distribution of the liquid is unknown, and
25 with multiple cloud layers it becomes difficult to partition the liquid among layers.
26 For this particular purpose, profiles where the ceilometer detected more than one
27 cloud base or the MMCR detected more than one cloud top were rejected. Out of the
28 3436 scanning radiometer profiles that are used for the main analysis, slightly less
29 than half, or 1611, represent single cloud layers and are used for the analysis of cloud
30 liquid and ice characteristics.

1 **3. Results**

2 **3.1 Cloud states**

3 Considering results based on the scanning radiometer alone, 40% of the cases are
4 decoupled while 28% are coupled and 32% are considered stable (Fig. 4, dark blue).
5 The corresponding results from the radiosonde profiles are 46% decoupled, 23%
6 coupled and 31% stable. The somewhat higher (lower) fraction of decoupled
7 (coupled) clouds for the radiosondes may be due to the inclusion of higher cloud
8 tops; as will be shown later, higher clouds are more likely to be decoupled than
9 lower ones. Considering the limited number of soundings available, the agreement is
10 reasonable and supports the use of the scanning radiometer profiles for the analysis.

11 Figure 4 also shows the relative frequency distributions (RFDs) of coupled,
12 decoupled and stable clouds for each period of ASCOS (see Section 2.1). Many deep
13 precipitating weather systems advected overhead from the beginning of the
14 expedition until the end of the 2nd ice drift period, and during the transition to the end
15 of ASCOS (Fig. 1). Hence there were only short and scattered occurrences of low
16 stratocumulus during these periods, which is why few profiles are included here.

17 From the beginning of ASCOS until the end of the 2nd period of the ice drift,
18 either stable or coupled clouds dominate when low-level stratocumulus are
19 intermittently present; nearly 80% of the profiles satisfying the geometric cloud
20 constraints described above during DoY 216-230 contain low clouds with tops below
21 500 m. The high fraction of stable clouds during this time is likely due to optically
22 and geometrically thin clouds; this will be investigated below. In the cases where a
23 cloud-driven mixed layer is observed, the proximity of these clouds to the surface
24 makes it easier for the cloud-generated motions to interact with surface-generated
25 turbulence (Shupe et al., 2013), which we speculate is the reason why decoupled
26 cases are rare during these early periods of ASCOS.

27 During the second period of the ice drift (DoY 230-234), higher clouds with
28 tops above 800 m in between the deeper precipitating systems are observed, which
29 are either decoupled or stable; however the latter is still the dominant state. During
30 the third period of the ice drift (DoY 234-236), the observed cloud states are either
31 coupled or stable, but now with coupled being the most frequent. This period is

1 dominated either by very low clouds or fog (95% of the profiles have a cloud top
2 below 400 m).

3 The fourth period of the ice drift (DoY 236-244) provides almost half of the
4 profiles included in this study. This is the longest period and also the one that was
5 examined by Shupe et al. (2013) and Sedlar and Shupe (2014) to study the cloud-
6 surface interactions and vertical velocity characteristics during ASCOS. The
7 persistent stratiform layer (Fig. 1) is often decoupled but intermittently connects
8 thermodynamically with the surface. Stable clouds are observed in only ~10% of
9 these profiles. Taking only the neutrally-stratified profiles into account, 74% are
10 found to be decoupled and 26% coupled; this is in very good agreement with the
11 occurrence statistics found in Shupe et al. (2013) and Sedlar and Shupe (2014).

12 During the fifth period (DoY 244-246), neutrally-stratified clouds still
13 dominate, although a considerable portion (~ 35%) of stable cases are also observed.
14 At the beginning of this period the stratiform cloud conditions from the previous
15 period persist, but are gradually decreasing in depth and height, becoming tenuous,
16 and at some points even dissipating (Fig. 1). Finally, from the transit period away
17 from the ice drift, few profiles are included because of the occurrence of several deep
18 precipitating weather systems. Most profiles are derived from DoY 246-248, when a
19 low stratiform cloud layer is observed, and from a few hours during DoY 249 and
20 251, when a very low tenuous cloud is apparent in the MMCR reflectivity (Fig. 1).

21 To summarize, the RFD of coupled, decoupled and stable cloud profiles
22 derived either from the scanning radiometer (Fig. 4) or the radiosonde (not shown)
23 reveals that neutrally-stratified clouds (coupled plus decoupled) are more frequent
24 during ASCOS than stable clouds. Yet, in the majority of the neutral cloud cases the
25 cloud-generated turbulence does not mix with the boundary layer below down to the
26 surface and the cloud remains decoupled. This is generally in agreement with Sedlar
27 and Shupe (2014) and Shupe et al. (2013), although the latter suggest an even higher
28 fraction of the neutrally stratified clouds to be decoupled; as shown above, this
29 difference is due to the different samples' size, while the use of different method
30 does not seem to affect the occurrence statistics.

31 The RFDs for cloud boundaries and cloud thickness are shown in Fig. 5. The
32 distribution of cloud top (Fig. 5a) indicates that clouds with tops above ~900 m are

1 usually decoupled while those with tops below ~ 500 m are coupled or stable. The
2 frequency distribution for cloud base (Fig. 5b) shows that coupled and stable clouds
3 have a cloud base below ~ 200 m during more than 50% of their occurrences,
4 whereas the decoupled cloud base distribution peak is much broader, between 400
5 and 800 m. In addition, the RFD for cloud thickness (Fig. 5c) indicates that stable
6 clouds are geometrically thinner than neutrally-stratified clouds, whereas decoupled
7 clouds are in general no thicker than the coupled clouds.

8 In summary, this analysis shows that stable clouds are geometrically thin and
9 low, while neutrally-stratified clouds are thicker with a tendency to have bases
10 higher above the surface. However, decoupled clouds appear higher up in the
11 atmosphere than coupled clouds; these results provide hints at the mechanism
12 explaining the different cloud classes. While turbulence is practically always
13 generated at the surface by mechanical mixing, unless very weak winds prevail,
14 strong radiative cooling at cloud top normally gives rise to buoyancy-generated
15 turbulence inside the cloud layer. In cases when the cloud layer is sufficiently close
16 to the surface, the two layers may interact, leading to a continuously coupled state.
17 On the other hand, when cloud layers are displaced higher, with cloud tops above
18 900 m, the in-cloud turbulence generated at the cloud top usually does not penetrate
19 to the surface-based mixed layer and thus becomes independent of the surface
20 conditions; the cloud state is decoupled. An exception to this description is a number
21 of low clouds that are not mixed at all (stable cloud states); these are about half of
22 the lowest and thinnest clouds, with cloud bases $< \sim 200$ m and thicknesses $< \sim 300$
23 m. This indicates that these thin clouds do not cool sufficiently to space at the top,
24 probably because they are either too optically thin or the liquid water content is
25 distributed rather homogeneously across the cloud layer, but also that the surface
26 generated turbulence is often too weak to mix clouds even when they lie below a few
27 hundred meters.

28 The relationship between cloud boundaries and the depth of the SCML is
29 further explored; it is found that the depth of the SCML increases as cloud base and
30 top heights increase (not shown). Yet, SCML depths are almost indifferent to cloud
31 thickness and increase only slightly with increasing cloud thickness; however, it must
32 be recalled that the range of thickness is similar for nearly all low-level cloud mixing

1 states (see Fig. 5c). The above general relationships were also observed by Shupe et
2 al. (2013), although for a shorter period, hence the results are not shown here.

3

4 **3.2 Surface fluxes**

5 The results in the previous section indicate that cloud-induced turbulence determines
6 coupling state, however, intuitively it would be reasonable to expect larger surface
7 fluxes to facilitate coupling to the surface. To examine the influence of the turbulent
8 surfaces fluxes on the cloud coupling state, RFDs of momentum, sensible and latent
9 heat fluxes for the three cloud coupling states are shown in Fig. 6. Upward fluxes are
10 positive; momentum flux is represented by the friction velocity which is always
11 positive. Turbulent heat fluxes are generally very small while the momentum fluxes
12 can be substantial (Tjernström et al. 2012). A comparison of the two time series
13 during times when they overlap (not shown) revealed relatively good agreement for
14 the momentum and sensible heat fluxes, whereas the latent heat fluxes exhibited
15 larger differences; see Section 2.2 for a discussion.

16 RFDs for momentum flux (Fig. 6a) show no significant difference among the
17 three cloud states, although the decoupled state has a broader peak over slightly
18 higher values. This is contrary to expectations; a larger momentum flux means more
19 mechanical mixing and, if it was important for the cloud state, less likely to be present
20 in a decoupled state. These distributions indicate that mechanical mixing is indeed not
21 a leading factor that determines coupling state. The same conclusion holds for the
22 sensible (Fig 6b) and latent (Fig 6c) heat fluxes, suggesting that surface turbulence is
23 not responsible for cloud-surface coupling states and that these interactions are thus
24 mainly driven by the cloud. This is in agreement with the results from Shupe et al.
25 (2013).

26

27 **3.3 Cloud water properties**

28 Cloud water properties are analyzed from single cloud-layer cases only; see Section
29 2.3. Of these 52% were decoupled, 31% coupled and 17% were stable. The lower
30 fraction of stable cases suggests that these are often present during occasions of
31 multiple cloud layers. However, the ratio between the two mixing states compares
32 favorably to the results from the whole period and those from only soundings.

1 The results in Fig. 7a are shown as box-and-whisker plots, and in Fig. 7b as
2 histograms. Negative (unphysical) LWP values included in the statistics are due to
3 the LWP uncertainty of $\sim 25 \text{ g m}^{-2}$ from the MWR instrument (see Section 2.2).
4 Figure 7a reveals that the stably-stratified cloud state is statistically different from
5 neutrally-stratified cloud states, since the LWP median ($\sim 32 \text{ g m}^{-2}$) is $\sim 50\%$ smaller
6 than the corresponding values for the latter states ($64 - 65 \text{ g m}^{-2}$); a student t-test
7 confirmed the significance of this difference at the 95% confidence level. Hence, the
8 initial hypothesis about the origin of the stable cases is supported; a cloud emits
9 radiation as a blackbody when LWP is larger than $\sim 30 - 50 \text{ g m}^{-2}$ (Stephens, 1978).
10 Cloud LWPs for the stable state are often at or below this blackbody emissivity
11 range, and it is likely that cloud-top radiative cooling, and hence buoyant mixing, is
12 reduced. The two neutrally-stratified cloud states exhibit no statistical difference,
13 suggesting that LWP by itself does not determine coupling state.

14 Histograms of LWP for the three cloud types (Fig. 7b) also indicate that the
15 stable cloud states in most cases are optically thin; 72% of the stable cloud profiles
16 have LWP observations below 50 g m^{-2} . Note, however, that even for the clouds that
17 contain enough liquid to be “blackbodies”, the buoyancy-generation of turbulence
18 depends on the differential cooling in the vertical. Thus, if liquid is homogeneously
19 distributed across the cloud then, instead of generating turbulence and mixing, the
20 whole cloud layer will cool. The RFDs for both neutrally-stratified states have peaks
21 between $50 - 80 \text{ g m}^{-2}$; decoupled clouds have the RFD peak shifted slightly to
22 higher values compared to the coupled clouds.

23 This result is contrary to that in Shupe et al. (2013), who found that coupled
24 clouds tend to have more LWP than decoupled; the reason may be the larger sample
25 in the present study. To investigate how the choice of a certain period of data affects
26 the statistical results, we calculated the LWP statistics for the 4th period of ASCOS
27 ice drift separately, the same period analyzed by Shupe et al. (2013), and compared
28 to the remaining periods. Considering only this period, the median LWP for coupled
29 clouds is $\sim 77 \text{ g m}^{-2}$ and its 25th percentile is $\sim 58 \text{ g m}^{-2}$, while for the remaining
30 periods it is ~ 58 and $\sim 43 \text{ g m}^{-2}$, respectively (not shown). This shows that coupled
31 cases during a persistent and relatively thick stratocumulus deck (Fig. 1) analyzed in
32 Shupe et al. (2013) contained relatively more liquid than during the other periods,

1 indicating the difference may lie in the differing time samples. This illustrates the
2 importance of having long time series for this type of analysis.

3 The results for the IWP (Fig. 8) also show that stable clouds differ from the
4 other two cloud types; stable cloud states have an IWP median around $\sim 0.5 \text{ g m}^{-2}$,
5 which is 4–6 times smaller than that for the neutrally-stratified cloud states, and
6 frequently has zero IWP. The medians for the coupled and decoupled states are
7 around ~ 3.2 and $\sim 2.7 \text{ g m}^{-2}$, respectively. The fact that stable cases have an IWP
8 close to zero indicates that these clouds are often not mixed-phase. Furthermore,
9 some of these stable clouds are probably cases of fog, consistent with their lower
10 cloud boundary statistics (see above).

11

12 **3.4 CCN concentrations**

13 Cloud formation depends on the presence of CCN; moreover, the concentration of
14 CCN strongly affects the optical properties of clouds and may impact on the cloud-
15 induced turbulence. Figure 9 illustrates near-surface CCN concentrations observed
16 during coupled, decoupled and stable states. The available CCN data corresponds to
17 the period between DoY 228-252, while during that time there are several short
18 periods where no data are available at all (e.g., due to pollution contamination by
19 ship exhaust; see Martin et al., (2011)). As a result, it is possible to match a CCN
20 concentration to a cloud state for only 25% of the total scanning radiometer profiles.
21 Also note that CCN is observed near the surface and that the observations may not
22 necessarily be representative for conditions in the cloud layer.

23 The median CCN concentration (Fig. 9) for stably-stratified clouds is $\sim 21 \text{ cm}^{-3}$
24 ³, whereas for neutrally-stratified cases the medians are twice as large, $\sim 43 - 44 \text{ cm}^{-3}$
25 ³. The low CCN concentrations explain the limited liquid amounts present in stable
26 clouds, thus providing additional support to the hypothesis that stable clouds are
27 optically thin; also see Mauritsen et al. (2011) that analyzed the effects of CCN
28 concentration on the optical properties of Arctic low-level clouds.

1 3.5 Vertical structure

2 To investigate the structure and phase of the clouds, RFDs of radar reflectivity as a
3 function of height are shown in Fig. 10. These results are shown on a scaled vertical
4 axis, which, by necessity, are slightly different for the three different cloud states;
5 each layer is scaled independently. For coupled clouds, $z_n=-1$ represents the
6 MMCR's first range gate, $z_n=0$ is the cloud base and $z_n=1$ the inversion base. Stable
7 cases are normalized in similar manner, except that $z_n=1$ is at the cloud top, since a
8 temperature inversion associated with the cloud top is not always present; note that
9 reflectivities above the cloud top are present in Fig. 12c, as a stricter definition on
10 radar reflectivity was used here to identify cloud boundaries, while the full
11 reflectivity profile was used for the statistics. Decoupled clouds have three layers;
12 the first range gate is at $z_n=-2$ while $z_n=-1$ is the decoupling height, $z_n=0$ the cloud
13 base and $z_n=1$ the inversion base. Heights above $z_n=1$ (the free troposphere) are also
14 scaled by the thickness of the layer below, since there is no other obvious scaling.

15 For coupled clouds (Fig. 10a) the range of reflectivity values extends from -40
16 dBZ to -5 dBZ, with a maximum frequency around -20 dBZ, throughout the whole
17 cloud, and almost the whole sub-cloud layer although the spread is larger here. A
18 rapid decrease is only observed close to the surface, where evaporation or
19 sublimation of precipitation takes place. Above the inversion base, the maximum
20 RFD remains constant to about $z_n \approx 1.3$, suggesting that the top of these clouds
21 usually extend into the inversion layer (cf. e.g., Sedlar and Tjernström, 2009; Sedlar
22 et al., 2012).

23 Decoupled clouds (Fig. 10b) have a similar structure to the coupled cases
24 inside the cloud, but exhibit a larger spread in reflectivity below cloud base. The
25 reflectivities of the layer between inversion base and cloud base extend from -40 dB
26 Z to -5 dB Z, whereas the values of the sub-cloud layer show an even larger spread
27 especially towards the smaller values (down to -65 dBZ). The RFD of the depth of
28 the SCML (not shown) revealed that it often varies between 200-600 m; thus, larger
29 variability in the sub-cloud layer reflectivity (Fig. 10b) may be due to different
30 features or characteristics of the decoupled cloud and/or sub-cloud layers depending
31 upon SCML depth.

1 The stable cases (Fig. 10c) are generally characterized by lower reflectivity
2 compared to the coupled cases. In the lower half of the cloud, reflectivity extends
3 between -50 dBZ and -15 dBZ, with a maximum frequency around -40 to -30 dBZ.
4 Below cloud base, the decrease in magnitude with decreasing height is more
5 pronounced than for coupled cases; the reflectivity is reduced by ~10 dBZ already at
6 $z_n \approx -0.3$, although the width of the distribution increases, explaining the more
7 gradual change in the median. In the upper half of the cloud, reflectivity decreases
8 rapidly with height. The in-cloud reflectivity values are often well below -17 dBZ, a
9 general upper limit of cloud droplet-only returns (Frisch et al. 1995), supporting the
10 hypothesis that stable clouds are not associated with appreciable precipitation.

11 In an attempt to investigate how the depth of the decoupled sub-cloud layer
12 correlates with the vertical structure of precipitation, we use the relationships
13 between the three radar moments at the decoupling height and the depth of the
14 SCML (Fig. 11). Figure 11a shows that reflectivity at the decoupling height
15 decreases gradually as the mixed layer deepens. For depths greater than 500 m, a
16 distinct peak in the RFD is apparent at very small reflectivities (< -50 dBZ).
17 Likewise, the RFD of Doppler spectrum width (Fig. 11c) also shows a decrease in
18 Doppler velocity variance for SCML depths $> \sim 300$ m. However, the Doppler
19 velocity distribution (Fig. 11b) at the decoupling height shows a slight tendency to
20 increase for SCML $> \sim 400$ m. This result appears to be inconsistent with the other
21 two radar moment distributions with SCML depth, as decreasing reflectivity and
22 reduced spectrum width tend to suggest a more homogeneous hydrometeor
23 distribution of generally smaller sizes. One possible explanation is that decreasing
24 reflectivity and spectrum width are affected by decreasing concentration of
25 precipitation, e.g. caused by sublimation of precipitation occurring in the deeper
26 SCMLs, but it is very difficult to deconvolve from the strong effect of size.
27 Nevertheless, all radar moments show a bimodality in RFD for the primary SCML
28 depths observed. To get a clearer distinction of the conditions that drive the
29 decoupling at different depths, we separate the decoupled clouds in two sub-
30 categories: those with a SCML depth less than 450 m and those with a SCML deeper
31 than 500 m; 60% and 30% of the total decoupled profiles respectively; clouds with a
32 shallower SCML hence occur twice as often as clouds with a deeper SCML.
33 Considering that increasing cloud boundaries correspond to increasing SCML depths

1 (section 3.1), the first category includes low decoupled clouds, whereas the latter
2 includes some of the highest clouds observed.

3 In Fig. 12, the reflectivity for decoupled clouds is shown again, but now
4 divided into the two categories. The decoupled clouds with the shallower SCML
5 (Fig. 12a) have a very similar structure to the coupled clouds (Fig. 12a). On the other
6 hand, decoupled clouds with a deeper mixed layer (Fig. 12b) differ substantially
7 from all the other cases: the maximum occurrence frequency close to the inversion
8 base is around -20 dBZ, same as for the coupled and decoupled clouds with shallow
9 SCML, but near cloud base it decreases to -30 dBZ. This is the only case where a
10 decrease inside the cloud layer is observed, suggesting that these clouds have little
11 ice, such that the reflectivity profile within the cloud is actually dominated by the
12 liquid. Furthermore, in the sub-cloud layer, reflectivity distribution is bimodal (Fig.
13 12b). In some cases it remains constant through cloud and upper sub-cloud layers,
14 very similar to coupled and decoupled cases with a shallower SCML; this branch in
15 the RFD however decreases and vanishes closer to the surface. The lack of values
16 below the decoupling height suggests that these profiles get decoupled around 100
17 m, the lowest vertical range gate of the MMCR. For the other mode, there is also a
18 decrease with decreasing height, from values < -40 dBZ below cloud base until the
19 decoupling height where the reflectivity minimum is reached, approaching -60 dBZ.
20 This illustrates the large potential impact on hydrometeors by
21 evaporation/sublimation, when precipitation falls through a relatively deep sub-
22 saturated layer below the cloud base.

23 Next the thermodynamic structures of the different (now four) cloud states are
24 analyzed. We did not find any relationship between cloud states and either cloud top,
25 cloud base or surface temperatures (not shown), so only the gradients of potential
26 temperature profiles are shown in Fig 13. Note, these are gradients of Θ profiles and
27 not Θ_E , on which the separation of coupled, decoupled and stable state was based.
28 Through the definition of Θ_E , an increase in Θ across a layer could be compensated
29 by a decrease in Q_v leading to a constant Θ_E ; hence, a thermodynamically coupled
30 case as defined using Θ_E could appear decoupled when using the Θ profile. Fig. 13,
31 showing the statistics of the Θ gradient profiles with respect to normalized height
32 (same as for radar reflectivity), reveals that this does not occur here.

1 In the coupled cases (Fig. 13a), the Θ gradient is slightly larger than zero in the
2 cloud, consistent with the release of latent heat in the cloud interior, and remains
3 almost constantly near-zero in the sub-cloud layer until the surface, where it
4 increases only slightly. In both the decoupled classes, two separate layers below the
5 cloud base are apparent. For the shallow SCML (Fig. 13b) category, the Θ gradient
6 is near-zero from inversion base until the decoupling height, followed by a weak
7 second inversion around the decoupling height and slightly stronger stability below.
8 Near the surface, the Θ gradient is near-zero or even slightly negative, suggesting the
9 existence of a turbulent surface layer.

10 For the decoupled state with a deeper SCML, however, the secondary
11 inversion is substantially more pronounced (Fig. 13c). Here the layer above the
12 decoupling height is also substantially less stable compared to the layer below. This
13 difference in thermal structure explains the separation between decoupled cloud
14 states with shallower or deeper SCML; it is actually a separation between states that
15 are “weakly” or “strongly” decoupled. Thus from here and onwards we will
16 examine four cloud states, using “weakly” and “strongly” decoupled, rather than
17 “shallow” or “deep”. In most stable cases (Fig. 13d), the near-surface structure is
18 somewhat more neutrally-stratified than aloft. The stratification is stable throughout
19 the profile and these clouds are hence also disconnected from the surface.

20 Figures 14 and 15 show normalized profile RFDs of mean Doppler velocity
21 and spectrum width. The median velocity profile for coupled clouds (Fig. 14a)
22 increases from the inversion base to close to the surface. In the cloud layer this
23 behavior is expected as hydrometeor sizes increase through collisions and diffusional
24 growth in the cloud interior, leading to larger hydrometeors with larger fall speeds.
25 In the sub-cloud layer, further increases in mean Doppler velocity indicate a
26 continued growth of the precipitation particles until approaching the surface. For the
27 weakly decoupled state (Fig. 14b) this increase stops near the decoupling height and
28 the Doppler velocity becomes constant below that level. For the strongly decoupled
29 clouds (Fig. 14c) the Doppler velocity increases abruptly slightly below the cloud
30 base and then becomes quasi-steady through the entire sub-cloud layer, including
31 above and below the decoupling height. The RFD maximum frequencies for these
32 cases are distributed around 0 m s^{-1} in the upper part of the cloud layer, suggesting
33 that the returns in this area are from the cloud liquid droplets. Moving downward in

1 the liquid layer the slowly increasing downward velocity is due to the fact that ice
2 starts to become relatively more abundant and more important for the total
3 backscatter. The quasi-constant Doppler velocity below the decoupling height is a
4 similar feature for both decoupled states; the ceased acceleration of hydrometeors at
5 the decoupling height could be connected with evaporation/sublimation occurring
6 locally. The stable cloud states (Fig. 14d) exhibit a totally different vertical structure
7 where Doppler velocity is distributed around zero throughout both cloud and sub-
8 cloud layer. The median profile is close to zero suggesting no, or very small, mean
9 vertical motions occur, in the cloud as well as the sub-cloud layer; this means that
10 clouds in the stable state have negligible precipitation.

11 The Doppler spectrum width (Fig. 15) is generally increasing from inversion
12 base down to cloud base for all cloud states, except for stable clouds (Fig 15d),
13 suggesting that with decreasing height, the variability in hydrometeor size also
14 increases within the cloud layer. Below cloud base, spectrum width decreases
15 downwards; this decrease is sharper for decoupled clouds and especially those that are
16 strongly decoupled (Fig. 15c). The rather quick decrease in spectrum width below the
17 cloud base in the latter cases is probably due to the fact that there is less ice
18 precipitation in these clouds and/or the deeper SCML allows for increased
19 sublimation of the smallest ice crystals, leading to a narrower Doppler spectrum.

20 Again, stable clouds (Fig. 15d) exhibit a completely different behavior than the
21 other cases. The larger spectrum width frequencies are distributed around 0.2 m/s
22 with an increasing spread towards higher values with decreasing height. These
23 substantially smaller values in the cloud layer, compared to the neutrally-stratified
24 clouds, are an additional indication that stable clouds are often not mixed-phase and
25 do not drive much turbulent mixing, while the slightly higher spread combined with
26 near zero average velocities indicates that the lower part of the sub-cloud layer is
27 slightly more turbulent than the cloud layer.

28 Profiles of relative humidity (with respect to ice, RH_i), specific moisture (Q_v)
29 and wind speed (U) (Figs. 16, 17 and 18) are analyzed from radiosoundings. Both Q_v
30 and U exhibited a significant scatter in absolute values, reflecting changes in air
31 mass, so a scaling method was applied: the scaled variables (U'' , Q_v'') are defined by
32 subtracting the mean values in the layer between the surface and inversion base (or
33 the cloud top for stable cases) from the actual values. RH_i is in a sense already a

1 scaled variable by definition and does not require any normalization. The RFDs of
2 the two scaled variables and RH_i are normalized with respect to height as previously.

3 The maximum frequency of RH_i is at or often above saturation in the cloud
4 interior for all states (Fig. 16). This indicates that these clouds can support the
5 coexistence of ice and liquid hydrometeors within the same volume, considering
6 layer mean temperatures are often below freezing. In the coupled and stable states
7 (Fig. 16 a, d) RH_i decreases below cloud base until the surface where it is sub-
8 saturated. This decrease is also observed in the decoupled cases (Fig. 16 b, c) but
9 only down to the decoupling height; below that level it either remains roughly
10 constant (Fig. 16b) or increases again (Fig. 16c). The decrease in RH_i below the
11 cloud base is the largest in the strongly decoupled cases (Fig. 16c) and a clear
12 minimum is observed around the decoupling height, below 85%. The generally
13 decreasing RH_i profile with decreasing height below cloud agrees with decreasing
14 profiles of Doppler spectrum widths and reflectivities, indicating sublimation of
15 falling ice crystals in the sub-cloud layer appears to be an ongoing process for the
16 majority of the strongly decoupled cloud states.

17 Specific humidity (Fig. 17) is similar in all states, except for the stable cases
18 (Fig. 17d), increasing with decreasing height from the inversion base until close to
19 the surface. For decoupled states, the structure below the decoupling height is
20 slightly different; specific humidity here is often quasi-constant, especially in the
21 strongly decoupled state where this layer is substantially moister in water vapor than
22 aloft (Fig. 17c); this moist environment could favor the formation of a lower
23 secondary cloud layer. Both coupled and decoupled cloud states (Fig. 17 a-c) show
24 that moisture increases above the temperature inversion near cloud top (e.g., Sedlar
25 and Tjernström 2009; Sedlar et al. 2012), indicating a potential source of moisture
26 for these cloud layers, by entrainment. While all neutrally-stratified cases have the
27 common feature of a general decrease in specific humidity with increasing height,
28 the stable clouds (Fig. 17d) feature the exact opposite behavior; a general increase
29 from near the surface to the cloud top. Only the layer close to the surface often
30 appears slightly more moist; however, the sub-cloud layer is still less moist than the
31 cloud layer and the air immediately above the cloud.

32 RFDs of wind speed profiles are given in Fig. 18. Wind speed is a highly
33 variable component of the system; hence the RFDs appear more scattered. The

1 median of coupled (Fig. 18a) and weakly decoupled clouds (Fig. 18b) are quite
2 similar, with almost constant wind speed inside the cloud and an increase from the
3 surface to the cloud base; for the coupled state, there is a very weak indication of a
4 maximum at the cloud base, agreeing with vertical wind speed shear during coupled
5 surface and cloud cases analyzed by Sedlar and Shupe (2014). In contrast, for the
6 strongly decoupled state (Fig. 18c), the median increases below cloud base and
7 reaches a maximum close to the decoupling height, and then decreases towards the
8 surface. Although this structure consists of many uniquely varying profiles, it
9 indicates the presence of low-level jets (LLJ) in some of them; the existence of these
10 LLJs might explain the slightly higher momentum fluxes observed earlier in the
11 decoupled cases (Fig. 6). The fact that the LLJ core occurs close to the decoupling
12 height, where an inversion usually exists (see Fig. 13c), has been also observed in
13 previous studies of nocturnal LLJs (Andreas et al., 2000; Jakobson et al., 2013).
14 Finally, for the stable cloud state (Fig. 18d), median wind speed is similar to the
15 coupled state, only the wind speed starts to decrease already from the cloud interior.
16 However, the bimodal structure of the RFD in the sub-cloud layer indicates the
17 potential presence of LLJs also here, with an occurrence of about half the time.

18

19

20 **4. Discussion**

21

22 Neutrally-stratified clouds are usually mixed-phase, precipitating clouds, more
23 frequently decoupled from the surface than coupled to it. In general, decoupled clouds
24 are higher than coupled; the analysis revealed that clouds with tops below 700 m tend
25 to get coupled to the surface, whereas those whose tops are above 900 m remain
26 decoupled from it. No differences were observed in geometric thickness or condensed
27 water properties between the two states.

28

29

30

31

32

Moreover, the surface fluxes are similar for both states, suggesting that the
observed cloud thermodynamic state is not driven by changes in the magnitude, or
sign, of the surface fluxes, in support of similar results in Shupe et al. (2013) and
Sedlar and Shupe (2014). It is more likely that displacements downwards (upwards)
of the cloud layer is the leading factor that results in coupling (decoupling), which

1 would instead be related more to the synoptic scale weather patterns and advected
2 thermodynamics (e.g., Sedlar and Shupe, 2014).

3 Decoupled clouds exhibit a differentiation in thermodynamic structure,
4 depending on the depth of the SCML; those with SCML less than 450 m are
5 disconnected from the surface by a weak inversion, whereas the clouds with SCML
6 greater than 500 m are characterized by stronger inversions at the decoupling height.
7 The “weakly decoupled” cases occur twice as often compared to the “strongly
8 decoupled”.

9 Apart from the thermodynamic differences between the coupled and the two
10 decoupled sub-categories, some microphysical differences were also observed. For
11 the strongly decoupled cases, the radar reflectivity profiles exhibit a decrease inside
12 the cloud, close to the cloud base and a bimodality in reflectivity distribution in the
13 sub-cloud layer. One branch of the distribution indicates a large reflectivity decrease
14 with decreasing height, suggesting that precipitation undergoes
15 evaporation/sublimation in the sub-cloud layer. In contrast, for coupled and weakly
16 decoupled cases the reflectivity remains almost constant throughout both cloud and
17 sub-cloud layer.

18 In addition, in strongly decoupled cases the sub-cloud mixed layer is
19 significantly drier; coupled and weakly decoupled RHi profiles decrease by only a
20 few percent in the sub-cloud layer, while in strongly decoupled profiles it reaches a
21 minimum around 85%. Moreover, RHi reaches its minimum at the decoupling height
22 and below that it increases again, suggesting that the vertical level at which the cloud
23 gets disconnected from the surface could be impacted by evaporation/sublimation.
24 This hypothesis is also supported by the fact that increasing mean Doppler velocity
25 with decreasing height ceases at the decoupling height in both decoupled sub-
26 categories, which suggests that the hydrometeors do not grow below that level; on the
27 contrary, in coupled cases the hydrometeors continue growing through the whole sub-
28 cloud layer.

29 Harrington et al. (1999) and Stevens et al. (1998), using modeling tools, suggest
30 that evaporation can promote decoupling, by cooling the sub-cloud layer and
31 stabilizing the atmosphere. Based on ASCOS observations, it seems unlikely that such
32 processes can be the primary reason driving the decoupling, since evidence of
33 sublimation was mainly found for strongly decoupled clouds, about 1/3 of all the total
34 decoupled profiles. Yet, we speculate that evaporation/sublimation may explain why

1 decoupling is amplified in these cases; for example, a strongly decoupled case may
2 occur because of the existence of a substantially warmer and moister layer capped by
3 the lower inversion, which releases upward latent heat flux, that probably helps in
4 sustaining the mixed layer over a larger depth above the decoupling height, as drier,
5 colder cloud-driven eddies come into contact with warmer and moisture air near the
6 decoupling height. On the other hand, the fact that precipitation falls through a deeper
7 layer might be the main reason why evaporation/sublimation appears more effective
8 in strongly decoupled cases, compared to the weakly decoupled.

9 To further support our speculations, we theoretically calculated the evaporating
10 rate that is required for a decoupling to occur. As a case study, we used a strongly-
11 decoupled profile (DoY 241, 11.31am) where the sub-cloud layer was disconnected
12 from the surface by a $\sim 1.5^{\circ}\text{C}$ strong inversion. Theoretical estimations revealed that
13 evaporation can cause a cooling of this magnitude within 1-3 hours, if evaporating
14 rates are $\sim 0.5\text{-}1.5\text{mm/day}$, assuming that all precipitation evaporates over a 100 m
15 deep layer. While precipitation rate is difficult to derive from our dataset, this simple
16 test shows that our argument that evaporating precipitation may enhance the
17 decoupling does not require excessive precipitation rates.

18 Other factors may also affect the stratification of the atmosphere, such as
19 horizontal advection in the sub-cloud layer. Furthermore, the fact that, in the strongly
20 decoupled cases, the layer capped by the inversion is often substantially moister than
21 the layer above, with RH reaching saturation, suggests that a secondary cloud layer
22 may be present; cloud radiative cooling at that level could also be related to the abrupt
23 change in stability observed in these cases.

24 Stably-stratified clouds differ substantially from the neutrally-stratified clouds;
25 they are geometrically the thinnest clouds observed and are also very low, usually
26 with a cloud base $< \sim 200$ m. The observed water properties indicate that these clouds
27 are optically thin, with few droplets; 72% of stable profiles have $\text{LWP} < \sim 50 \text{ g m}^{-2}$,
28 suggesting that stable clouds do not contain enough liquid to drive efficient in-cloud
29 mixing, whereas the IWP is close to zero, indicating that they are often liquid only,
30 or at least with very few ice crystals. For the remaining stable cases, that have
31 sufficient amount of liquid to produce turbulent motions, the main unanswered
32 question is the distribution of the liquid water in the vertical, e.g. the liquid water
33 content profile. One possibility is that the liquid may not be concentrated near cloud
34 top but rather be distributed more homogeneously across the cloud, so that differential

1 cooling within the cloud layer is inhibited, as hypothesized by Sedlar et al. (2012) for
2 the portion of cloud layers that extend into the temperature inversion. Moreover, the
3 CCN concentrations are small for the stable clouds, further supporting that the
4 majority of stable clouds are optically thin; this assumes that the CCN concentrations
5 observed near the surface are representative of the in-cloud conditions which may
6 not be the case neither when the entire surface-to-cloud layer is stably-stratified nor
7 when the clouds are decoupled.

8 The potential temperature gradient profiles in these stable cases show that
9 surface turbulence usually does not impact the stable clouds and the specific
10 humidity profiles, with increasing moisture with increasing height, indicate that the
11 surface does not serve as a moisture source. The observed Doppler velocities are
12 close to zero suggesting that these clouds are often non-precipitating. The
13 magnitudes of the Doppler spectrum width are very small, which also supports the
14 conclusion that stable clouds are usually not mixed-phase and have little turbulence.

15 The question remains why these stable clouds contain only liquid. The low
16 CCN concentration with the optically thin stable clouds is an indication that the air
17 mass for these cases has a low aerosol concentration and it is not unreasonable to
18 expect that this would also mean that IN concentrations are small; Prenni et al.
19 (2007) showed that the concentration of IN is critical to the formation of ice crystals.
20 The fact that IWP is low in these cases may thus be related to the aerosol
21 characteristics. Mauritsen et al. (2011) studied such a case from ASCOS in detail.
22 They hypothesize that, due to the low CCN concentration, the optically thin cloud
23 consists of a small number of relatively large droplets eventually so large that they
24 sediment out of the cloud, hence feeding back on the low CCN concentration. The
25 presence of large spherical droplets is borne out by the frequent occurrence of so-
26 called fog-bows - a halo-like optical phenomenon that only occurs with relatively
27 large (20-50 μm) spherical droplets (Lee, 1998).

28 The statistical approach of this study does not allow a study of development over
29 time; to further investigate the possible evolution of these clouds we performed a few
30 case studies, based both on cases with very low LWP and slightly higher LWP,
31 $\sim 15\text{g/m}^2$ and $\sim 65\text{g/m}^2$, respectively (not shown). Based on these studies it appears
32 that when the LWP is very low, the cloud slowly becomes more and more tenuous
33 and eventually dissipates; the time for this can be anywhere from half a day up to

1 two days; this is consistent with the hypothesis in Mauritsen et al. (2011). In the case
2 with more liquid water, the cloud becomes thicker over time growing upwards and
3 eventually the stably-stratified profile gradually changes into a neutrally-stratified
4 profile and, within hours it gets coupled to the surface as in-cloud turbulence starts.
5 In this case a moisture inversion is present and it is hypothesized the cloud has a
6 homogenous distribution of liquid across its layer as described above, which
7 prevents destabilization of the cloud layer. As it grows up into the moisture
8 inversion, the water supply from this is assumed to cause additional condensation
9 and a redistribution of the liquid in the cloud layer, allowing differential cooling to
10 occur, which eventually leads to the generation of cloud driven turbulence.

11 Hence, two possible paths for the evolution of stable cloud state appear to be
12 supported: (1) the thinner clouds become more and more tenuous until they dissipate
13 completely. (2) the somewhat thicker clouds increase in optical thickness or achieve
14 changes in the vertical distribution of liquid through more liquid condensate; this
15 allows them to eventually drive turbulent motions which may connect with surface-
16 generated turbulence, considering that the stable clouds are often in very close
17 proximity to the surface (~below 200 m) – thus eventually transitioning to a coupled
18 cloud state.

19

20 **5. Conclusions**

21 Arctic low-level clouds and Arctic boundary layer structure have been examined,
22 using observations from the ASCOS expedition, in late summer 2008. In particular,
23 this study focuses on the interactions between low-level clouds and the surface.
24 Profiles of equivalent potential temperature are used to identify neutrally-stratified
25 clouds that are thermodynamically “coupled” to, or “decoupled” from, the surface
26 turbulence. Apart from these two cases, where turbulence is generated inside the
27 cloud, a significant number of stably-stratified cases are also identified, suggesting the
28 absence of in-cloud mixing for these cases. The vertical structure and properties of
29 these three types: decoupled, coupled and stable clouds, is investigated. This study
30 shows that:

1 • Decoupled clouds occur more frequently than coupled. The coupling state is
2 primarily driven by the cloud, through turbulence generated in the cloud by
3 radiative cooling and buoyant processes and is determined by the proximity of the
4 cloud layer to the surface mixed layer. Surface fluxes seem to simply respond to
5 the cloud processes aloft.

6

7 • Decoupled clouds exhibit a bimodality in thermodynamic structure, associated
8 with the depth of the sub-cloud mixed layer (SCML); clouds with shallower
9 SCMLs are weakly decoupled from the surface, whereas higher clouds with
10 relatively deeper SCMLs are strongly decoupled. The enhancement of the
11 decoupling for the cases with a deeper SCML is possibly due to
12 evaporation/sublimation of precipitation occurring within the SCML.

13

14 • Stable clouds differ substantially from all neutrally-stratified states in both
15 thermodynamic and microphysical structure, as well as in geometry and water
16 properties. They are geometrically and optically thin clouds, often single-phase
17 (liquid) with no or negligible precipitation. Some of these cases, based on their
18 proximity to the surface and tenuous nature, represent fog.

19

20 Further testing of these conclusions and potential links between the in-cloud
21 dynamics and the cloud and precipitation microphysics, including feedbacks and
22 forcing of the thermodynamic structure, should be further explored using modeling
23 tools (e.g., Solomon et al., 2011; Solomon et al., 2014) Also, while this study
24 illustrates the power of surface based remote sensing techniques, more direct in-situ
25 profiling of both turbulence and cloud microphysics from the surface and through the
26 clouds, to determine the nature of the coupling, would be highly advantageous.

27 **References**

28 ACIA: Impacts of a warming Arctic: Arctic Climate Impact Assessment. Cambridge

- 1 University Press, 2005.
- 2 Andreas, E. L., K. J. Claffey, and Makshtas A. P.: Low-level atmospheric jets and
3 inversions over the western Weddell Sea. *Bound. Layer Meteor.*, 97, 459–486, doi
4 10.1023/A:1002793831076, 2000.
- 5
- 6 Andreas, E.L., Jordan, R.E., Makshtas, A.P.: Parameterizing turbulent exchange over
7 sea ice: the ice station weddell results. *Bound. Layer Meteor.*, 114,439–460, doi
8 10.1007/s10546-004-1414-7, 2005.
- 9 Bigg, E. K. and Leck, C.: Cloud-active particles over the central Arctic Ocean, *J.*
10 *Geophys. Res.*, 106 (D23), 32155–32166, doi 10.1029/1999JD901152, 2001.
- 11 Bintanja, R., van der Linden, E., and Hazeleger, W.: Boundary layer stability and
12 Arctic climate change: A feedback study using EC-Earth, *Clim. Dynam.* 39, 2659–
13 2673, doi 10.1007/s00382-011-1272-1, 2012.
- 14 Bony, S., and J.L. Dufresne: Marine boundary layer clouds at the heart of tropical
15 cloud feedback uncertainties in climate models. *Geophys. Res. Lett.*, 32, L20806, doi
16 10.1029/2005GL023851, 2005.
- 17 Comiso, J.C.: A rapidly declining Arctic Perennial Ice Cover. *Geophys Res. Lett.*, 29,
18 1956, doi 10.1029/2002GL015650, 2002.
- 19 Curry, J.A.: Interactions among turbulence, radiation and micro-physics in Arctic
20 stratus clouds. *J. Atmos. Sci.*, 43, 90–106, doi 10.1175/1520-0469,1986.
- 21 Curry, J.A. and Ebert, E.E.: Annual cycle of radiative fluxes over the Arctic Ocean:
22 Sensitivity to cloud optical properties. *J. Clim.*, 5, 1267-1280, doi 10.1175/1520-
23 0442(1992)0052.0.CO;2, 1992.
- 24 Curry, J.A., Rossow, W.B., Randall, D., Schramm, J. L.: Overview of Arctic cloud
25 and radiation characteristics. *J. Clim.*, 9,1731–1764, doi 10.1175/1520-
26 0442(1996)009<1731:OOACAR>2.0.CO;2, 1996.
- 27 Devasthale, A., Sedlar, J., Koenigk, T., and Fetzer, E. J.: The thermodynamic state of
28 the Arctic atmosphere observed by AIRS: comparisons during the record minimum
29 sea ice extents of 2007 and 2012, *Atmos. Chem. Phys.*, 13, 7441-7450, doi
30 10.5194/acp-13-7441-2013, 2013.
- 31 Frisch, A.S., Fairall, C.W., Snider, J.B.: Measurement of stratus cloud and drizzle
32 parameters in ASTEX with a K_{α} -band doppler radar and a microwave radiometer. *J*
33 *Atmos. Sci.*, 52:2788–2799, doi 10.1175/1520-0469(1995)0522.0.CO;2, 1995.
- 34 Graverson R.G., Mauritsen T., Tjernström M., Källén E., Svensson G.: Vertical

1 structure of recent Arctic warming. *Nature* 451:53–57, doi 10.1038/nature06502,
2 2008.

3 Harrington, J.Y., Reisin, T., Cotton, W.R., and Kreidenweis, S.M.: Cloud resolving
4 simulations of Arctic stratus - Part II: Transition-season clouds, *J. Atmos. Res.*, 51,
5 45-75, doi 10.1016/S0169-8095(98)00098-2, 1999.

6 Intrieri, J.M., Shupe, M.D., Uttal, T., and McCarty, B.J.: An annual cycle of Arctic
7 clouds characteristics observed by radar and lidar at SHEBA, *J. Geophys. Res.*,
8 107, doi 10.1029/2000JC000423, 2002.

9 Jakobson, L., Vihma, T., Jakobson, E., Palo, T., Männik, A., and Jaagus, J.: Low-level
10 jet characteristics over the Arctic Ocean in spring and summer, *Atmos. Chem. Phys.*
11 *Discuss.*, 13, 2125-2153, doi 10.5194/acpd-13-2125-2013, 2013.

12 Kahl, J.D., Serreze, M.C., and Schnell, R.C.: Low-level tropospheric temperature
13 inversions in the Canadian Arctic, *Atmosphere-Ocean*, 30, 511-529, doi
14 10.1080/07055900.1992.9649453, 1992.

15 Karlsson, J., and Svensson, G.: The simulation of Arctic clouds and their influence on
16 the winter surface temperature in present-day climate in the CMIP3 multi-model
17 dataset. *Clim. Dyn.*, 36, 623–635, doi 10.1007/s00382-010-0758-6, 2010.

18 Kapsch, M., Graverson, R.G., Tjernström, M.: Springtime atmospheric energy
19 transport and the control of Arctic summer sea-ice extent . *Nature Clim. Change*, doi
20 10.1038/nclimate1884, 2013.

21 Kay, J.E., and Gettelman, A.: Cloud influence on and response to seasonal Arctic sea
22 ice loss. *J. Geophys. Res.*, 114, D18204, doi 10.1029/2009JD011773, 2009.

23 Korolev A.: Limitations of the Wegener–Bergeron–Findeisen mechanism in the
24 evolution of mixed-phase clouds. *J. Atmos. Sci.*, 64 (9), 3372–5, doi
25 10.1175/JAS4035.1, 2007.

26 Lauer, A., K. Hamilton, Y. Wang, V.T.J. Phillips, and R. Bennartz: The Impact of
27 Global Warming on Marine Boundary Layer Clouds over the Eastern Pacific – A
28 Regional Model Study. *J. Climate*, 23 (21), 5844-5863, doi 10.1175/2010JCLI3666.1,
29 2010.

30 Leck, C., Norman, M., Bigg, E. K., and Hillamo, R.: Chemical composition and
31 sources of the high Arctic aerosol relevant for fog and cloud formation, *J. Geophys.*
32 *Res.*, 107, D12, 4135, doi 10.1029/2001JD001463, 2002.

33 Leck, C., Tjernström, M., Matrai, P., Swietlicki, E., Bigg, K.: Can marine micro-
34 organisms influence melting of the Arctic pack ice? *EOS* 85, 25–36, doi
35 10.1029/2004EO030001, 2004.

- 1 Lee, R. L.: Mie theory Airy theory and the natural rainbow, *Appl. Opt.*, 37(9), 1506-
2 1519, doi 10.1364/AO.37.001506, 1998.
- 3 Lindsay, R. W., Zhang, J., Schweiger, A. J., and Steele, M. A., and Stern, H.: Arctic
4 sea ice retreat in 2007 follows thinning trend. *J. Clim.*, 22, 165-176, doi
5 10.1175/2008JCLI2521, 2009.
- 6 Mahrt, L., Heald, R. C., Lenschow, D. H., Stankov, B. B., and Troen, I.: An
7 observational study of the structure of the nocturnal boundary layer. *Bound. Layer*
8 *Meteor.*, 17, 247–264, doi 10.1007/BF00117983, 1979.
- 9 Martin, M., Chang, R. Y.-W., Sierau, B., Sjogren, S., Swietlicki, E., Abbatt, J. P. D.,
10 Leck, C., and Lohmann, U.: Cloud condensation nuclei closure study on summer
11 arctic aerosol, *Atmos. Chem. Phys.*, 11, 11335-11350, doi 10.5194/acp-11-11335-
12 2011, 2011.
- 13 Maslanik, J. A., C. Fowler, J. Stroeve, S. Drobot, J. Zwally, D. Yi, and W. Emery. A
14 younger, thinner Arctic ice cover: Increased potential for rapid, extensive sea-ice loss.
15 *Geophys. Res. Lett.*, 34, L24501, doi 10.1029/2007GL032043, 2007.
- 16 Mauritsen, T., Sedlar, J., Tjernström, M., Leck, C., Martin, M., Shupe, M.,
17 Sjogren, S., Sierau, B., Persson, P. O. G., Brooks, I. M., and Swietlicki, E.: An Arctic
18 CCN-limited cloud-aerosol regime, *Atmos. Chem. Phys.*, 11, 165-173, doi
19 10.5194/acp-11-165-2011, 2011.
- 20 Moran, K.P., Martner, B.E., Post, M.J., Kropfli, R.A., Welsh, D.C., and Widener,
21 K.B.: An unattended cloud-profiling radar for use in climate research. *Bull. Amer.*
22 *Meteor. Soc.*, 79, 443- 455, doi 10.1175/1520-0477(1998)0792.0.CO;2, 1998.
- 23 Morrison, H., de Boer, G., Feingold, G., Harrington, J., Shupe, M. D., and Sulia, K.:
24 Resilience of persistent Arctic mixed-phase clouds, *Nat. Geo.*, 5, 11–17, doi
25 10.1038/NGEO1332, 2012.
- 26 Nghiem, S. V., Rigor, I. G., Perovich, D. K., Clemente-Colon, P., Weatherly, J. W.,
27 and Neumann, G.: Rapid reduction of Arctic perennial sea ice, *Geophys. Res. Lett.*,
28 34, L19504, doi 10.1029/2007GL031138, 2007.
- 29 Nicholls, S.: The dynamics of stratocumulus: Aircraft observations and comparisons
30 with a mixed layer model. *Q.J.R. Meteorol. Soc.*, 110 : 783–820. doi 10.1002/
31 /qj.49711046603, 1984.
- 32 Overland, J. E., Spillane, M. C., Percival, D. B., Wang, M., and Mofjeld, H. O.:
33 Seasonal and regional variation of pan-Arctic surface air temperature over the
34 instrumental record, *J. Clim.*, 15, 3263–3282, doi 10.1175/1520-
35 0442(2004)0172.0.CO;2, 2004.

- 1 Perovich, D.K., Richter-Menge, J.A., Jones, K.F., Light, B.: Sunlight, water, and ice:
2 extreme Arctic sea ice melt during the summer of 2007. *Geophys. Res. Lett.*
3 35:L11501, doi 10.1029/2008GL034007, 2008.
- 4 Persson P.O.G., Fairall C.W., Andreas E.L., Guest P.S., Perovich D.K.:
5 Measurements near the Atmospheric Surface Flux Group tower at SHEBA: Near-
6 surface conditions and surface energy budget. *J. Geophys. Res.* 107(8045):1–21, doi
7 10.1029/2000 JC000705, 2002.
- 8 Pinto, J.O. and Curry, J.A.: Atmospheric convective plumes emanating from leads: 2.
9 Microphysical and radiative processes. *J. Geophys. Res.*, 100, 4633-4642, doi
10 10.1029/94JC02655, 1995.
- 11 Pinto, J.O.: Autumnal mixed-phase cloudy boundary layers in the Arctic. *J. Atmos.*
12 *Sci.*, 55, 2016–2038, doi 10.1175/1520-0469(1998)0552.0.CO;2, 1998.
- 13 Pithan, F. and Mauritsen, T.: Arctic amplification dominated by temperature
14 feedbacks in contemporary climate models. *Nature Geosci.*, doi: 10.1038/NGEO2071,
15 2014.
- 16 Prenni, A. J., DeMott, P. J., Kreidenweis, S. M, Harrington, J. Y., Avramov, A.,
17 Verlinde, J., Tjernström, M., Long, C. N., and Olsson, P. Q.: Can Ice-Nucleating
18 Aerosols Affect Arctic Seasonal Climate? *Bull. Amer. Meteor. Soc.*, 88, 541–550, doi
19 10.1175/BAMS-88-4-541, 2007.
- 20 Randall, D., Curry, J., Battisti, D., Flato, G., Grumbine, R., Hakkinen, S., Martinson,
21 D., Preller, R., Walsh, J., and Weatherly, J.: Status of and outlook for large-scale
22 modeling of atmosphere-ice-ocean interaction in the Arctic. *Bull. Amer. Meteor. Soc.*,
23 79,197-219, doi 10.1175/1520-0477(1998)0792.0.CO;2, 1998.
- 24 Roberts, G. C. and Nenes, A. A: continuous-flow streamwise thermal-gradient CCN
25 chamber for atmospheric measurements, *Aerosol Sci. Technol.*, 39, 206–221, doi
26 10.1080/027868290913988, 2005.
- 27 Richter-Menge, J.: The Arctic. [in “State of the Climate in 2009”]. *Bull. Amer.*
28 *Meteor. Soc.*, 91, 107-124, 2010.
- 29 Sedlar, J. and Tjernström, M.: Stratiform Cloud-Inversion Characterization During the
30 Arctic Melt Season, *Bound. Layer. Meteorol.*, 132, 455-474, doi 10.1007/s10546-009-
31 9407-1, 2009.
- 32 Sedlar, J., Tjernström, M., Mauritsen, T., Shupe, M.D., Brooks, I.M., Persson, P.O.G.,
33 Birch, C.E., Leck, C., Sirevaag, A., and Nicolaus, M.: A transitioning Arctic surface
34 energy budget: the impacts of solar zenith angle, surface albedo and cloud radiative
35 forcing. *Clim. Dyn.*, 37, 1643–1660, doi 10.1007/s00382-010-0937-5, 2011.

- 1 Sedlar, J., Shupe, M. D., and Tjernström, M.: On the relationship between
2 thermodynamic structure, cloud top, and climate significance in the Arctic, *J. Clim.*,
3 25, 2374–2393, doi 10.1175/JCLI-D-11-00186.1, 2012.
- 4 Sedlar J. and Shupe, M.D.: Characteristic nature of vertical motions observed in
5 Arctic mixed-phase stratocumulus, *Atmos. Chem. Phys.*, 14, 3461-3478, doi
6 10.5194/acp-14-3461-2014, 2014.
- 7 Serreze, M. C., Walsh, J. E., Chapin III, F. S., Osterkamp, T., Dyurgerov, M.,
8 Romanovsky, V., Oechel, W. C., Morison, J., Zhang, T., and Barry, R.G.:
9 Observational evidence of recent change in the northern high-latitude environment.
10 *Clim. Change*, 46, 159–207, doi 10.1023/A:1005504031923, 2000.
- 11 Serreze, M. C. and Francis, J. A.: The arctic amplification debate. *Clim. Change*, 76
12 (3-4): 241-264, doi 1007/s10584-005-9017-y, 2006.
- 13 Serreze, M.C., Holland, M.M., and Stroeve, J.: Perspectives on the Arctic's shrinking
14 sea-ice cover. *Science*, 315, 1533 – 1536, doi 10.1126/science. 1139426, 2007.
- 15 Serreze, M. C., and Barry, R. G.: Processes and impacts of Arctic amplification: A
16 research synthesis. *Global and Planetary Change* 77: 85-96, doi 10.1016/
17 j.gloplacha.2011.03.004, 2011.
- 18 Shupe, M.D., and Intrieri, J.M.: Cloud radiative forcing of the Arctic surface: The
19 influence of cloud properties, surface albedo, and solar zenith angle, *J. Clim.*, 17, 616-
20 628, doi 10.1175/1520-0442(2004)0172.0.CO;2, 2004.
- 21 Shupe, M.D., Uttal, T., and Matrosov, S.Y.: Arctic cloud microphysics retrievals from
22 surface-based remote sensors at SHEBA. *J. Appl. Meteor. Clim.*, 44, 1544-1562, doi
23 0.1175/JAM2297.1, 2005.
- 24 Shupe, M.D., Kollias, P., Persson, P.O.G., McFarquhar, G.M.: Vertical motions in
25 Arctic mixed-phase stratiform clouds. *J. Atmos. Sci.*, 65, 1304–1322,
26 10.1175/2007JAS2479.1, 2008.
- 27 Shupe, M.D., Walden, V.P., Eloranta, E., Uttal, T., Campbell, J R., Starkweather,
28 S.M., and Shiobara, M.: Clouds at Arctic Atmospheric Observatories, Part I:
29 Occurrence and macrophysical properties. *J. Appl. Meteor. Clim.*, 50, 626-644, doi
30 10.1175/2010JAMC2467.1, 2011.
- 31 Shupe, M. D.: Clouds at Arctic Atmospheric Observatories, Part II: Thermodynamic
32 phase characteristics. *J. Appl. Meteor. Clim.*, 50, 645-661, doi
33 10.1175/2010JAMC2468.1, 2011.
- 34 Shupe, M. D., Persson, P. O. G, Brooks, I. M., Tjernström, M., Sedlar, J. ,Mauritsen,
35 T. ,Sjogren, S. and Leck, C.: Cloud and boundary layer interactions over the Arctic

1 sea-ice in late summer. *Atmos. Chem. Phys. Discuss.*, 13, 5, 13191-13244, doi
2 10.5194/acp-13-9379-2013, 2013.

3 Simmonds, I. and Rudeva, I.: The great Arctic cyclone of August 2012, *Geophys.*
4 *Res. Lett.*, 39, L23709, doi 10.1029/2012GL054259, 2012.

5 Sirevaag, A., de la Rosa, S., Fer, I., Nicolaus, M., Tjernström, M., and McPhee, M.
6 D.: Mixing, heat fluxes and heat content evolution of the Arctic Ocean mixed layer.
7 *Ocean Sci.*, 7, 335–349, doi 10.5194/os-7-335-2011, 2011.

8 Solomon, A., Shupe, M. D., Persson, P. O. G., and Morrison, H.: Moisture and
9 dynamical interactions maintaining decoupled Arctic mixed-phase stratocumulus in
10 the presence of a humidity inversion, *Atmos. Chem. Phys.*, 11, 10127-10148, doi
11 10.5194/acp-11-10127-2011, 2011.

12 Solomon, A., Shupe, M. D., Persson, P. O. G., Morrison, H., Yamaguchi, T.,
13 Caldwell, P. M., and de Boer, G.: The Sensitivity of Springtime Arctic Mixed-Phase
14 Stratocumulus Clouds to Surface-Layer and Cloud-Top Inversion-Layer Moisture
15 Sources. *J. Atmos. Sci.*, 71, 574–595, doi: [http://dx.doi.org/10.1175/JAS-D-13-](http://dx.doi.org/10.1175/JAS-D-13-0179.1)
16 0179.1, 2014.

17 Stephens, G.L.: Radiation profiles in extended water clouds. II. Parameterization
18 schemes. *J. Atmos. Sci.*, 35, 2123–2132, doi 10.1175/1520-0469(1978)0352.0.CO;2,
19 1978.

20 Stevens, B., Cotton, W. R., Feingold, G., and Moeng, C.-H: Large-Eddy Simulations
21 of Strongly Precipitating, Shallow Stratocumulus-Topped Boundary Layers, *J. Atmos.*
22 *Sci.*, 55, 3616-3638, doi 10.1175/1520-0469(1998)0552.0.CO;2, 1998.

23 Stroeve, J., Holland, M., Meier, W., Scambos, T., and Serreze, M.: Arctic sea ice
24 decline: faster than forecast, *Geophys. Res. Lett.*, 34, L09501, doi
25 10.1029/2007GL029703, 2007.

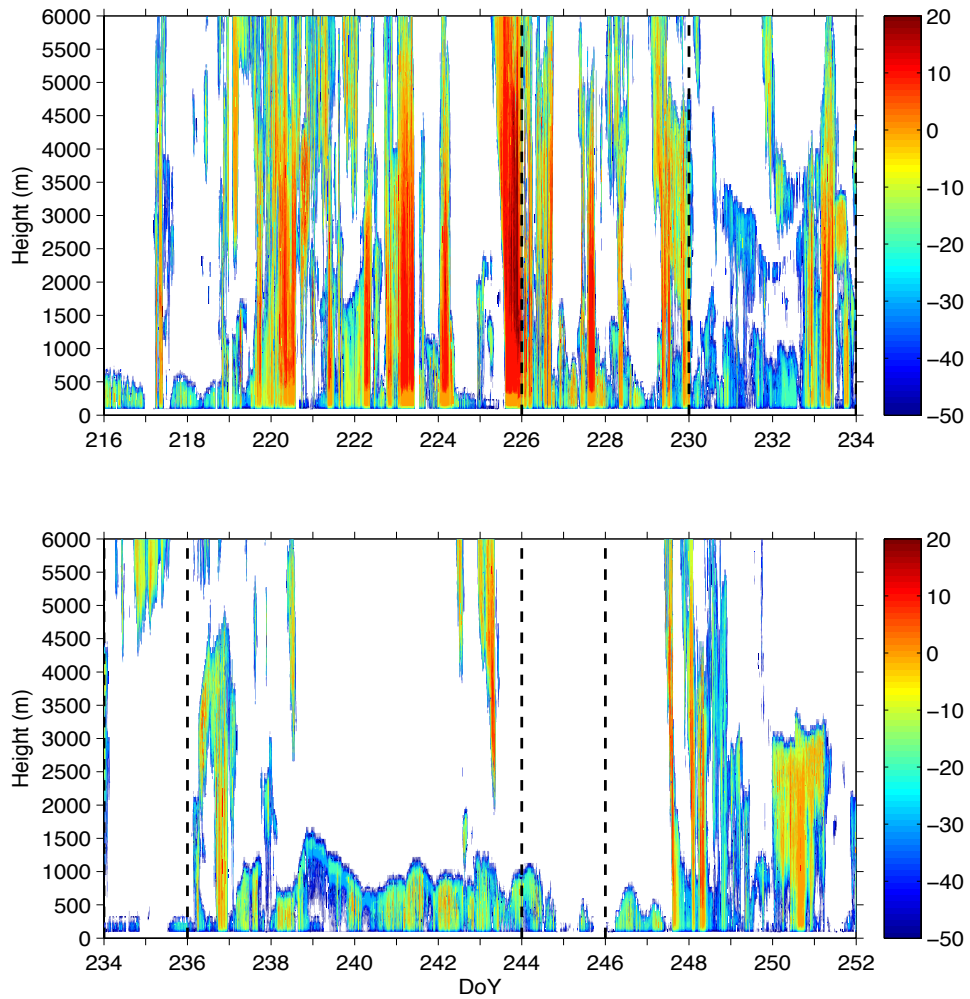
26 Stroeve, J. C., Serreze, M. C., Holland, M. M., Kay, J. E., Malanik, J., and Barrett, A.
27 P.: The Arctic’s rapidly shrinking sea ice cover: a research synthesis, *Clim. Change*,
28 110, 1005–1027, doi 10.1007/s10584-011-0101-1, 2012.

29 Tjernström, M., Leck, C., Persson, P.O.G., Jensen, M. L., Oncley, S.P. and Targino,
30 A.: The summertime Arctic atmosphere: Meteorological measurements during the
31 Arctic Ocean Experiment (AOE-2001). *Bull Amer. Meteor. Soc.*, 85, 1305-1321, doi
32 10.1175/BAMS-85-9-1305, 2004a.

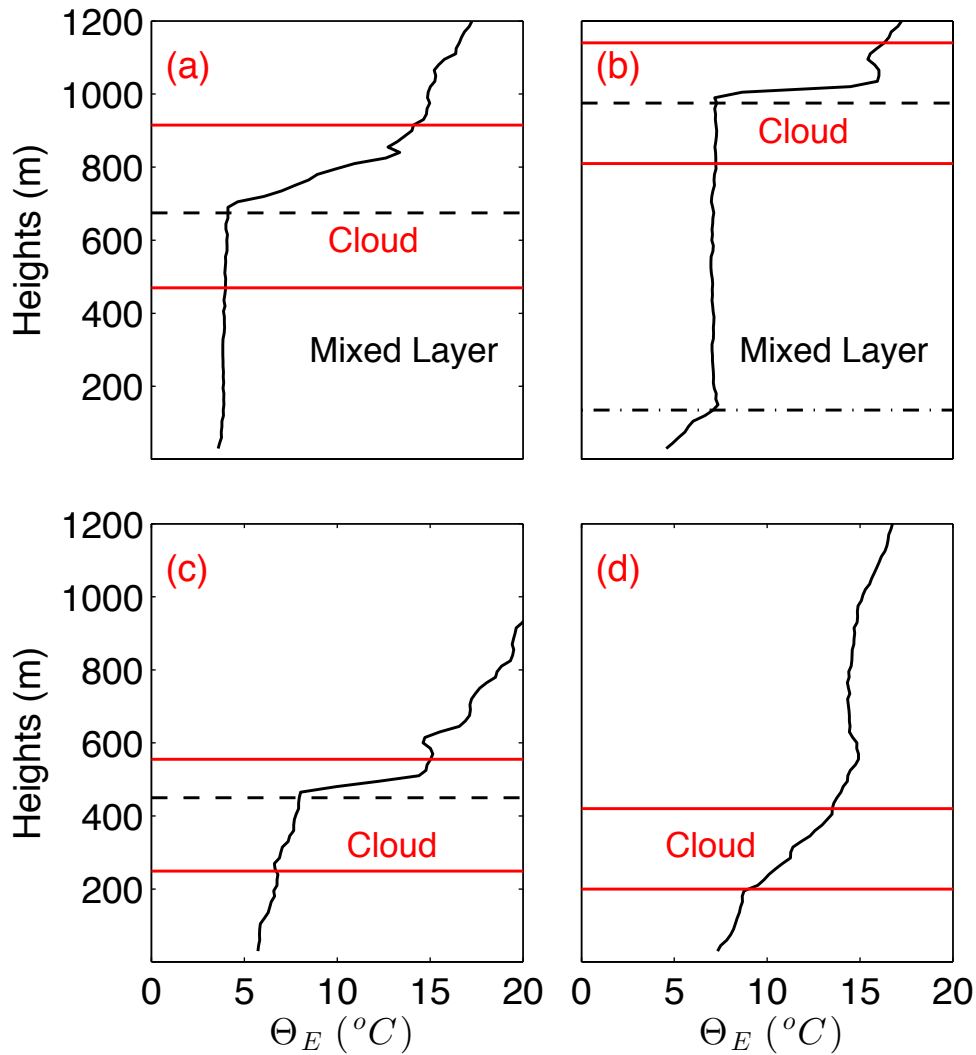
33 Tjernström, M., Leck, C., Persson, P.O.G., Jensen, M. L., Oncley, S.P. and Targino,
34 A.: Experimental equipment: An electronic supplement to “The summertime Arctic
35 atmosphere: Meteorological measurements during the Arctic Ocean Experiment
36 (AOE-2001)”. *Bull Amer. Meteor. Soc.*, 85, 1322–1322, doi 10.1175/BAMS-85-9-

- 1 Tjernstrom, 2004b.
- 2 Tjernström, M.: The summer Arctic boundary layer during the Arctic Ocean
3 Experiment 2001 (AOE-2001). *Bound. Layer Meteorol.*, 117, 5-36, doi
4 10.1007/s10546-004-5641-8, 2005.
- 5 Tjernström, M., Zagar, M., Svensson, G., Cassano, J.C., Pfeifer, S., Rinke, A., Wyser,
6 K., Dethloff, K., Jones, C. Semmler, T., and Shaw, M.: Modelling the Arctic
7 boundary layer: An evaluation of six ARCMIP regional-scale models using data from
8 the SHEBA project. *Bound. Layer Meteorol.*, 117, 337-381, doi 10.1007/s10546-004-
9 7954-z, 2005.
- 10 Tjernström, M., Sedlar, J., and Shupe, M.D.: How well do regional climate models
11 reproduce radiation and clouds in the Arctic?, *J. App. Meteorol. Clim.*, 47, 2405-
12 2422, doi 10.1175/2008JAMC1845.1, 2008.
- 13 Tjernström, M., Birch, C. E., Brooks, I. M., Shupe, M. D., Persson, P. O. G.,
14 Sedlar, J., Mauritsen, T., Leck, C., Paatero, J., Szczodrak, M., and Wheeler, C. R.:
15 Meteorological conditions in the central Arctic summer during the Arctic Summer
16 Cloud Ocean Study (ASCOS), *Atmos. Chem. Phys.*, 12, 6863-6889, doi 10.5194/acp-
17 12-6863-2012, 2012.
- 18 Tjernström, M., Leck, C., Birch, C. E., Bottenheim, J. W., Brooks, B. J., Brooks, I.
19 M., Bäcklin, L., Chang, R. Y. W., Granath, E., Graus, M., Hansel, A., Heintzenberg,
20 J., Held, A., Hind, A., de la Rosa, S., Johnston, P., Knulst, J., Westberg, M., de
21 Leeuw, G., Di Liberto, L., Martin, M., Matrai, P. A., Mauritsen, T., Müller, M.,
22 Norris, S. J., Orellana, M. V., Orsini, D. A., Paatero, J., Persson, P. O. G., Gao, Q.,
23 Rauschenberg, C., Ristovski, Z., Sedlar, J., Shupe, M. D., Sierau, B., Sirevaag, A.,
24 Sjogren, S., Stetzer, O., Scietlicki, E., Szczodrak, M., Vaattovaara, P., Wahlberg, N.,
25 and Wheeler, C. R.: The Arctic Summer Cloud Ocean Study (ASCOS): Overview and
26 experimental design, *Atmos. Chem. Phys.*, 14, 2823-2869, doi 10.5194/acp-14-2823-
27 2014, 2014.
- 28 Twomey, S.A.: The influence of pollution on the shortwave albedo of clouds, *J.*
29 *Atmos. Sci.*, 34, 1149-1152, doi 10.1175/1520-0469(1977)0342.0.CO;2, 1977.
- 30 Uttal, T., Curry, J.A., Mcphee, M.G., Perovich, D.K., Moritz, R.E., Maslanik, J.A.,
31 Guest, P.S., Stern, H.L., Moore, J.A., Turenne, R., Heiberg, A., Serreze, M.C., Wylie,
32 D.P., Persson, P.O.G., Paulson, C.A, Halle, C., Morison, J.H., Wheeler, P.A.,
33 Makshtas, A., Welch, H., Shupe, M.D., Intrieri, J.M., Stamnes, K., Lindsey, R.W.,
34 Pinkel, R., Pegau, W.S., Stanton, T.P., Grenfeld, T.C.: Surface Heat Budget of the
35 Arctic Ocean, *Bull. Amer. Meteor. Soc.*, 83, 22 255-276, doi 10.1175/1520-
36 0477(2002)083<0255:SHBOTA>2.3.CO;2, 2002.
- 37 Wang, X., and Key, J.R.: Arctic Surface, Cloud, and Radiation Properties Based on
38 the AVHRR Polar Pathfinder Data Set. Part I: Spatial and Temporal Characteristics, *J.*

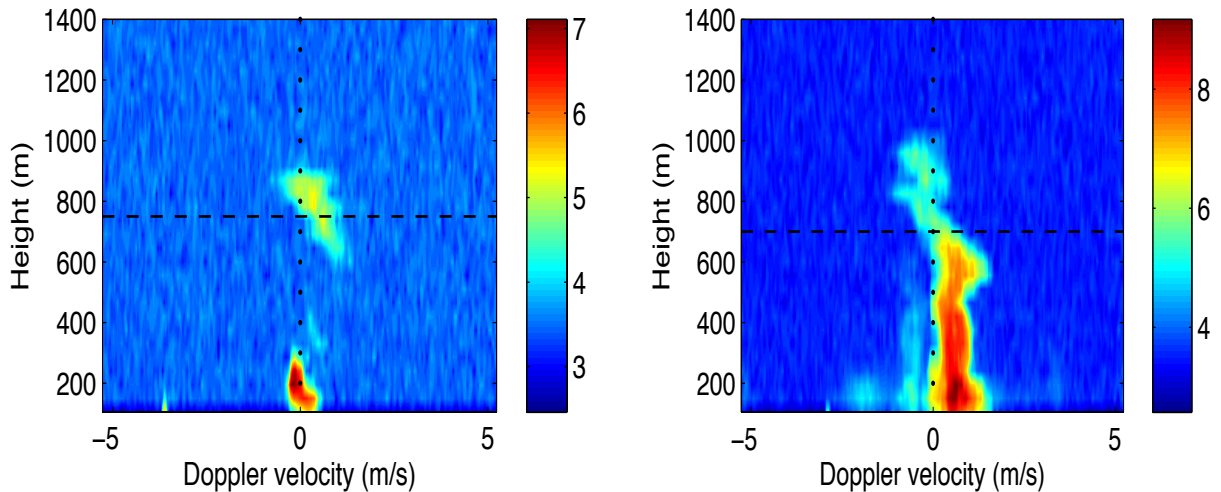
- 1 Clim., 18, 30 2558-2574, doi 10.1175/JCLI3438.1, 2005.
- 2 Webb, M. J., C. A. Senior, D. M. H. Sexton, W. J. Ingram, K. D. Williams, M. A.
3 Ringer, B. J. McAvaney, R. Colman, B. J. Soden, R. Gudgel, T. Knutson, S. Emori,
4 T. Ogura, Y. Tsushima, N. Andronova, B. Li, I. Musat, S. Bony, K. E. Taylor: On the
5 contribution of local feedback mechanisms to the range of climate sensitivity in two
6 GCM ensembles *Clim. Dyn.* 27 17–38, doi 10.1007/s00382-006-0111-2, 2006.
- 7 Westwater, E.R., Han, Y., Irisov, V. G., Leuskiy, V., Kadyrov, E. N., and Viazankin,
8 S. A.: Remote sensing of boundary layer temperature profiles by a scanning 5-mm
9 microwave radiometer and RASS: Comparison experiments. *J. Atmos. Ocean. Tech.*,
10 16, 805 – 818, doi 10.1175/1520-0426(1999)0162.0.CO;2, 1999.
- 11 Westwater, E.R., Han, Y., Shupe, M.D., Matrosov, S.Y.: Analysis of integrated cloud
12 liquid and precipitable water vapor retrievals from microwave radiometers during
13 SHEBA, *J. Geophys. Res.*, 106, 32,019-32,030, doi 10.1029/2000JD000055, 2001.
- 14 Zhang, J., Lindsay, R., Schweiger, A., and Steele, M.: The impact of an intense
15 summer cyclone on 2012 Arctic sea ice retreat, *Geophys. Res. Lett.*, 40, 720–726, doi
16 10.1002/grl.50190, 2013.



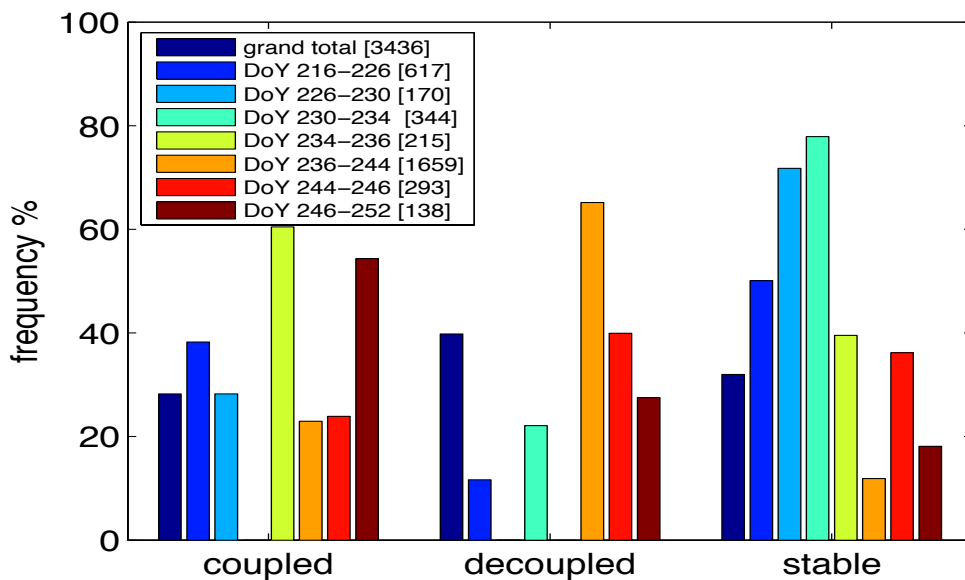
1 Figure 1: Radar reflectivity contour [colors, dBZ] time-series for the ASCOS
 2 experiment, given in Day of Year (DoY) 2008. The vertical dashed lines differentiate
 3 the five periods of the ice drift (see section 2.3 for a discussion on period
 4 characteristics). Periods prior to DoY 226 and after DoY 246 are the transit periods
 5 (before/after the ice drift). Reflectivity profiles are shown up to 6 km.



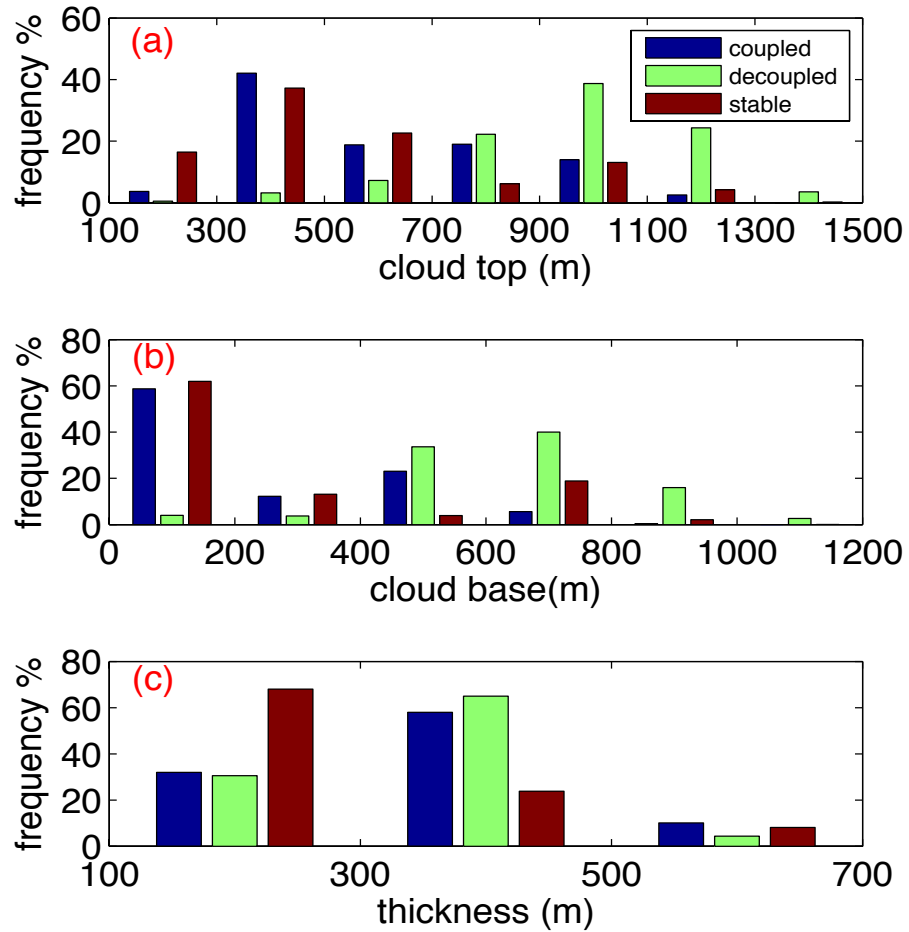
1 Figure 2: Example profiles of scanning radiometer equivalent potential temperature
 2 (Θ_E) [$^{\circ}\text{C}$] vertical profiles from four ASCOS cases: (a) coupled cloud [DoY 240,
 3 20:16:47 pm], (b) decoupled cloud [DoY 239, 16:51:47 pm], (c) stable cloud (with
 4 inversion identified around cloud top) [DoY 217, 16:45:00 pm], (d) stable cloud (no
 5 inversion around cloud top) [DoY 251, 02:43:13 am]. Red lines indicate the
 6 respective cloud boundaries observed at profile time. The inversion base height is
 7 shown as the black dashed line. The black dashed-dotted line indicates the decoupling
 8 height. The layer between dashed and dashed-dotted, or the surface, is defined as the
 9 mixed layer.



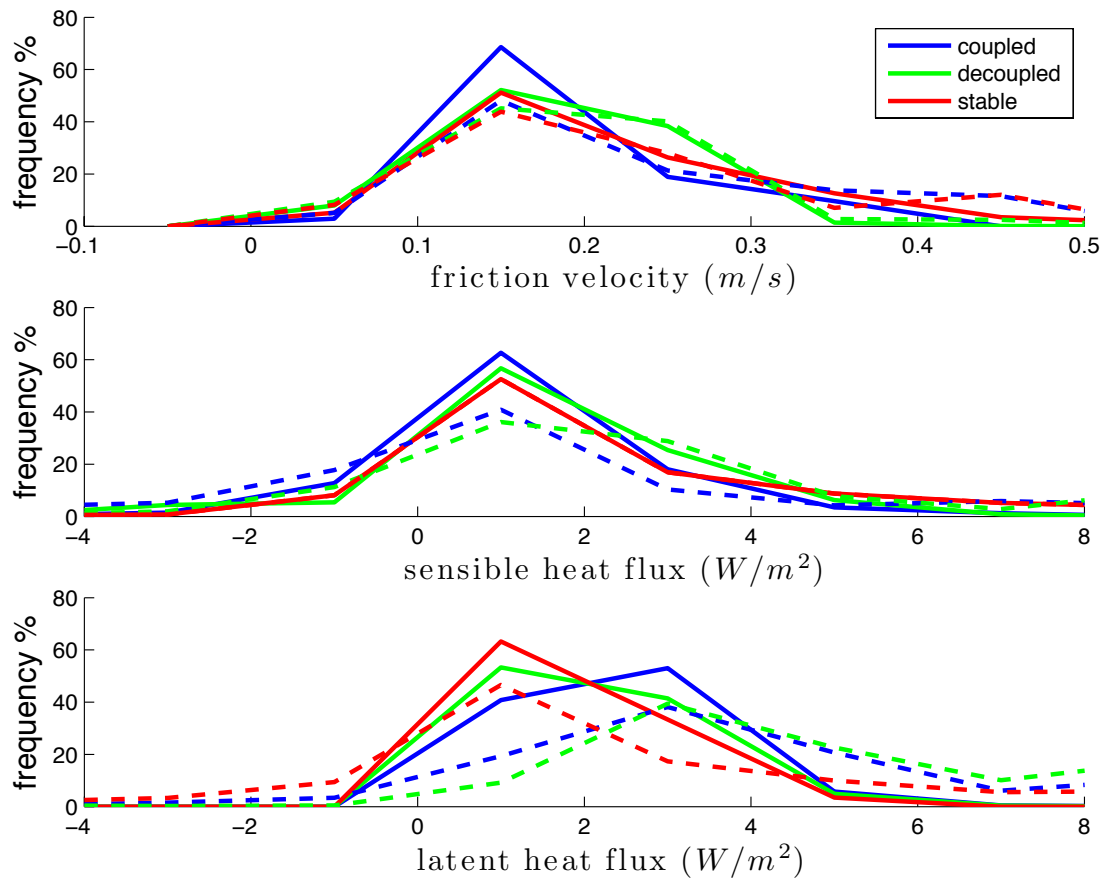
1 Figure 3: Spectrographs for two ASCOS snapshots: (a) DoY 241, 19:11:52 pm: The
 2 cloud top median height observed by the MMCR is 960 m and the median cloud base
 3 height observed by the ceilometer is 90 m. We estimate the upper cloud base at 750 m
 4 from the spectrograph. (b) DoY 237, 10:11:40 am: The cloud top median height is
 5 1095 m and ceilometer median cloud base height is 140 m. We estimate the real base
 6 at 700 m. The horizontal black dashed lines indicate the qualitatively derived cloud
 7 base heights. Colors show the relative frequency distribution (logarithm of reflectivity
 8 counts) of spectral density of Doppler velocity with height. Positive (negative) values
 9 represent downward (upward) motion. Zero values are highlighted with dots.



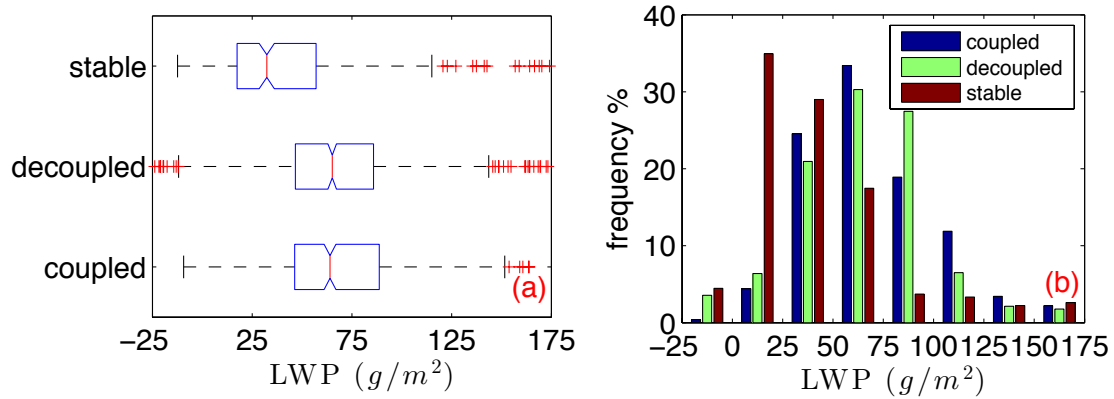
10 Figure 4: Relative frequency distribution (RFD) of cloud state occurrence for each
 11 period of ASCOS. The number in the brackets indicates the total number of scanning
 12 radiometer profiles analyzed for each period of ASCOS (see section 2.3 for a
 13 discussion on period characteristics).



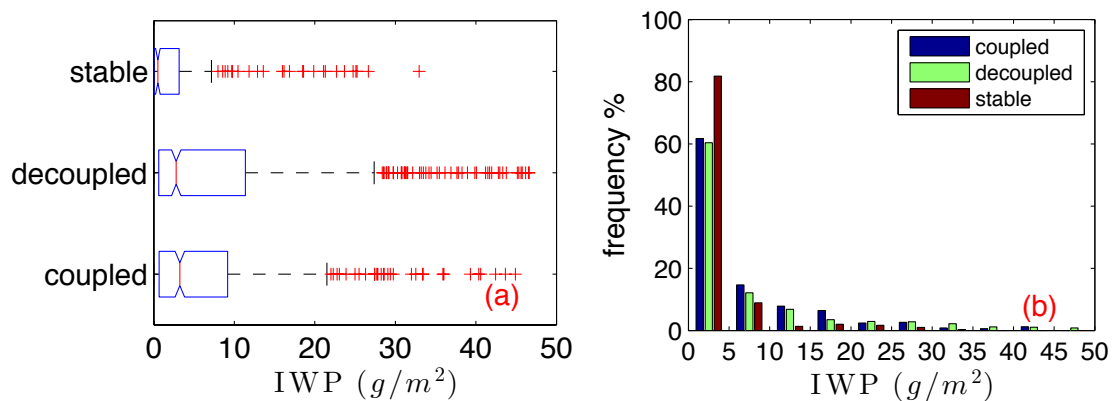
1 Figure 5: RFDs of (a) cloud top height [m], (b) cloud base height [m] and (c) cloud
 2 thickness [m] for coupled (blue), decoupled (green) and stable (red) cloud states. Bin
 3 size is 200 m and centered in the interval.



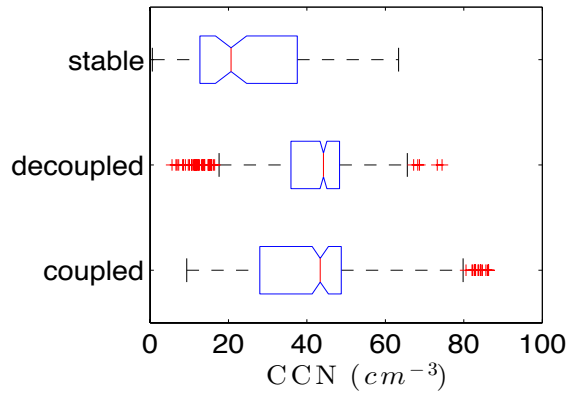
1 Figure 6: RFDs of (a) friction velocity [m s^{-1}] representing momentum flux, (b)
 2 sensible heat flux [W m^{-2}] and (c) latent heat flux [W m^{-2}] for coupled (blue),
 3 decoupled (green) and stable (red) clouds. Solid lines represent fluxes estimated from
 4 sonic anemometers while dotted lines are the bulk fluxes; see Section 2.2 for a
 5 description on flux calculations.



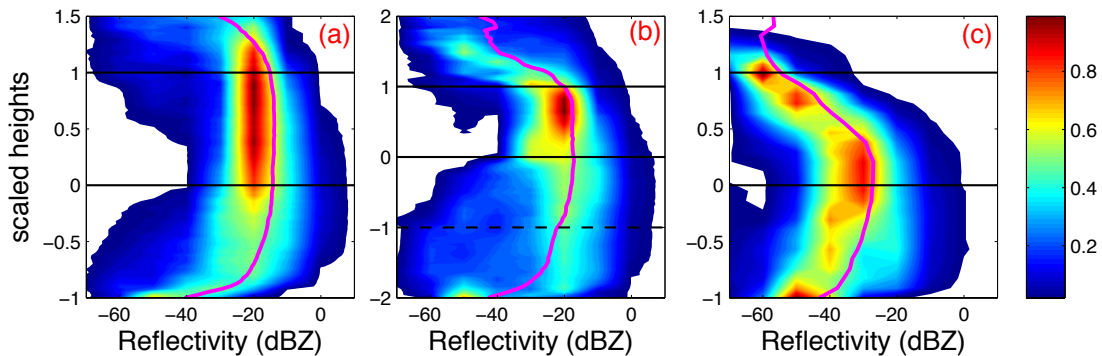
1 Figure 7: (a) Notched box-and-whisker plots and (b) RFDs of LWP [$g\ m^{-2}$] for
 2 coupled, decoupled and stable single cloud layers. In (a), median values are indicated
 3 by the red solid line, edges of the box mark the lower and upper quartiles, whiskers
 4 represent the extent of the data that is 1.5 times the difference between the upper and
 5 lower quartile and crosses are outliers. Notches offer a rough guide to significance of
 6 difference of medians; the width of the notches is proportional to the interquartile
 7 range of the sample and inversely proportional to the square root of the size of the
 8 sample. The bin size in (b) is $25\ g\ m^{-2}$ and centered in the interval. Negative values
 9 are due to the instrument uncertainty of $25\ g\ m^{-2}$.



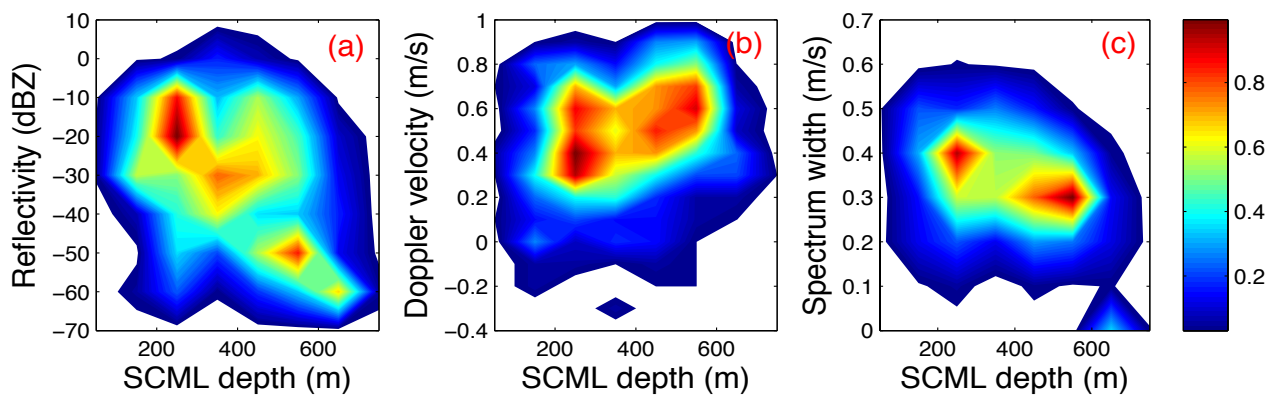
10 Figure 8: Same as in Fig. 9, but for ice water path (IWP) [$g\ m^{-2}$] derived from radar
 11 power-law relationships. The bin size in (b) is $5\ g\ m^{-2}$ and centered in the interval.



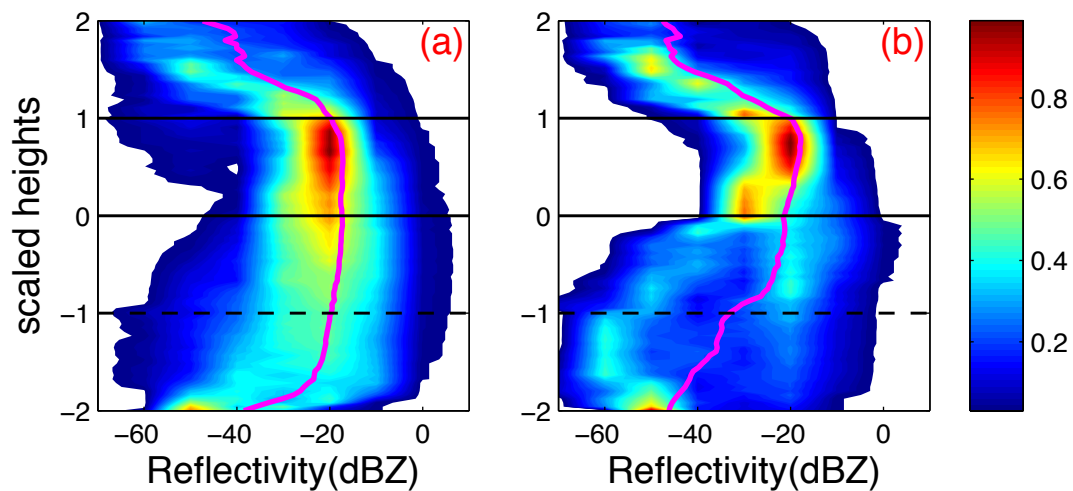
1 Figure 9: Notched box-and-whisker plot of CCN concentrations [cm^{-3}] for coupled,
 2 decoupled and stable cloud layers. CCN concentrations are measured from ship level
 3 (see Martin et al., 2011).



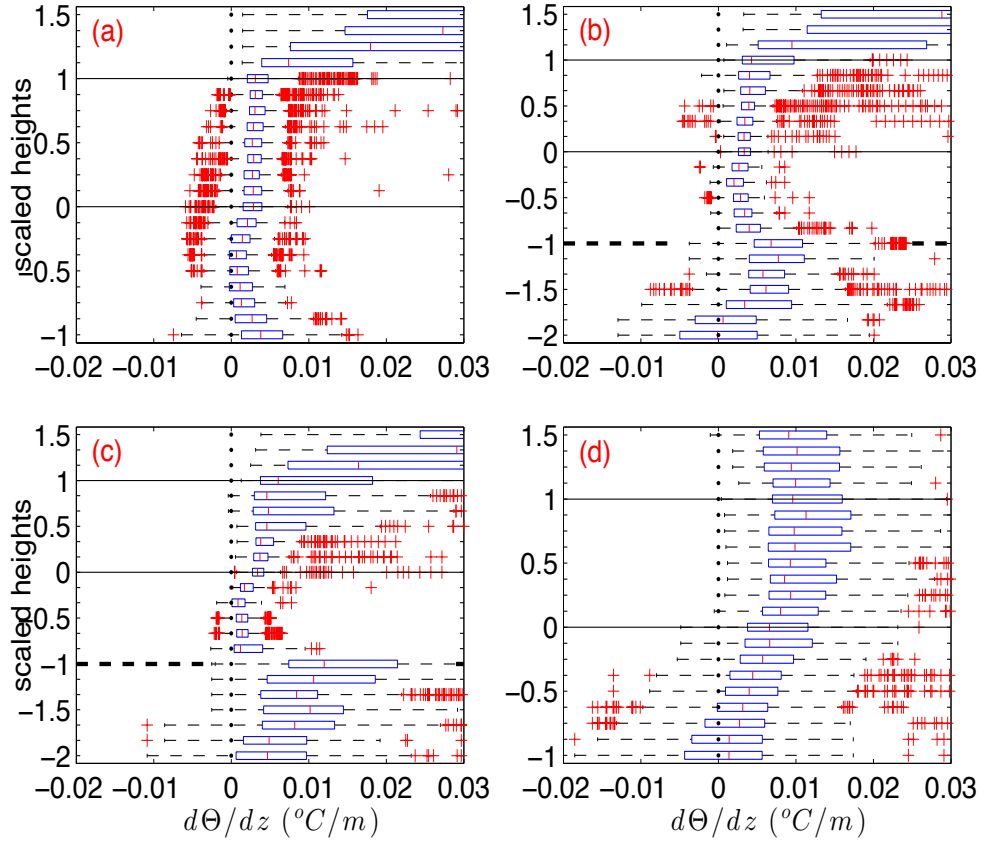
4 Figure 10: RFD contour plots of radar reflectivity [dBZ] for (a) coupled, (b)
 5 decoupled and (c) stable clouds; magenta profiles are the medians. Heights are
 6 normalized: for (a) coupled clouds, $z_n=-1$ is the first range gate, $z_n=0$ is cloud base and
 7 $z_n=1$ is the main inversion base; for (b) decoupled clouds, $z_n=-2$ is the first range gate,
 8 $z_n=-1$ is the decoupling height, $z_n=0$ is cloud base and $z_n=1$ is main inversion base; for
 9 (c) stable clouds, $z_n=-1$ is the first range gate, $z_n=0$ is cloud base and $z_n=1$ is cloud top;
 10 reflectivity values above cloud top ($z_n=1$) for (c) occur because stricter reflectivity
 11 thresholds were applied to identify cloud boundaries, while the full reflectivity
 12 profiles were used to compute the histogram statistics. Frequencies are normalized by
 13 unity (unity indicates the maximum frequency of all levels).



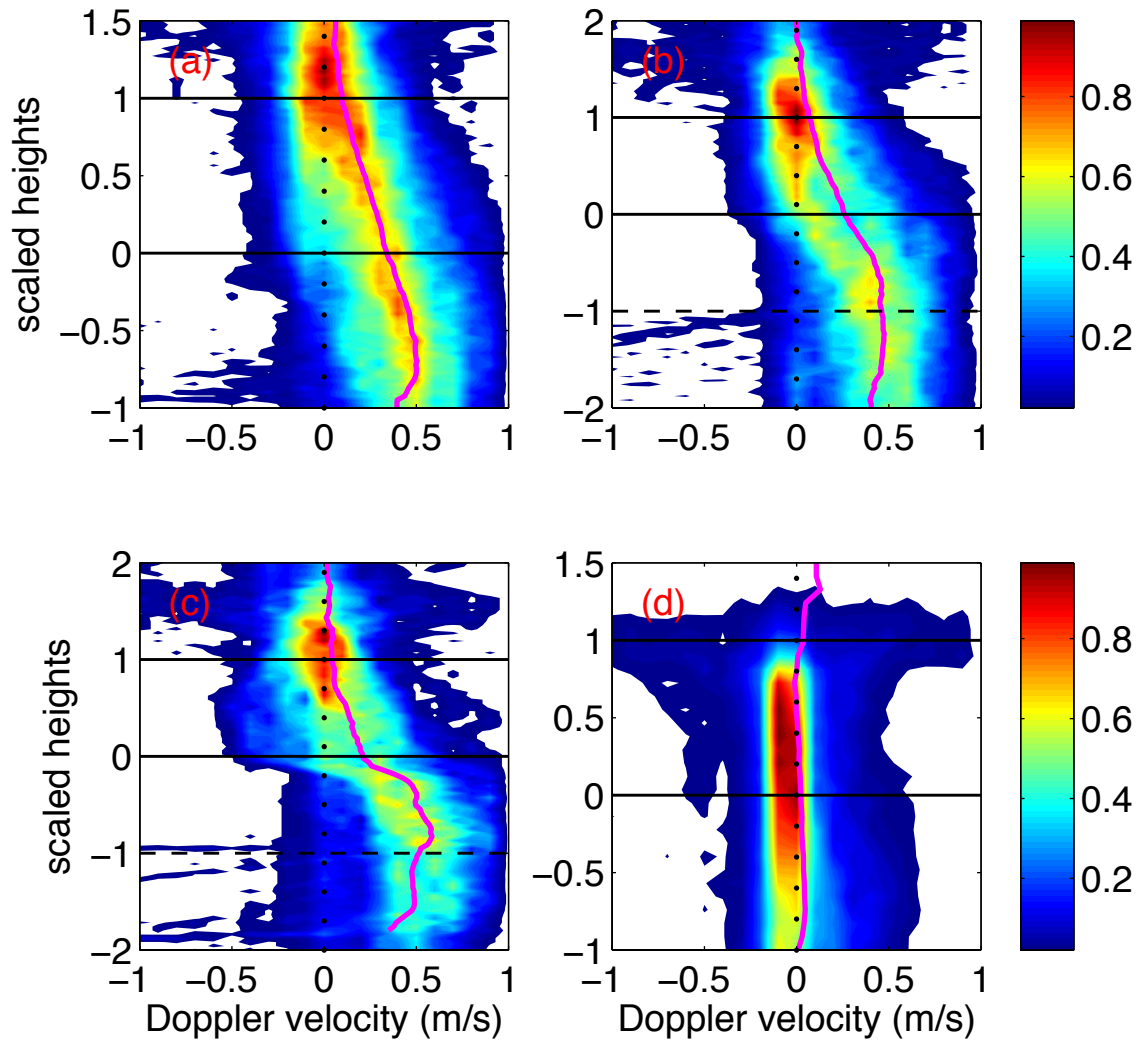
1 Figure 11: 2-D RFD contour plots of (a) radar reflectivity [dBZ], (b) Doppler
 2 velocity [m s^{-1}] and (c) spectrum width [m s^{-1}] at the decoupling height, in
 3 relationship to the sub-cloud mixed layer (SCML) depth [m]. Frequencies are
 4 normalized by unity.



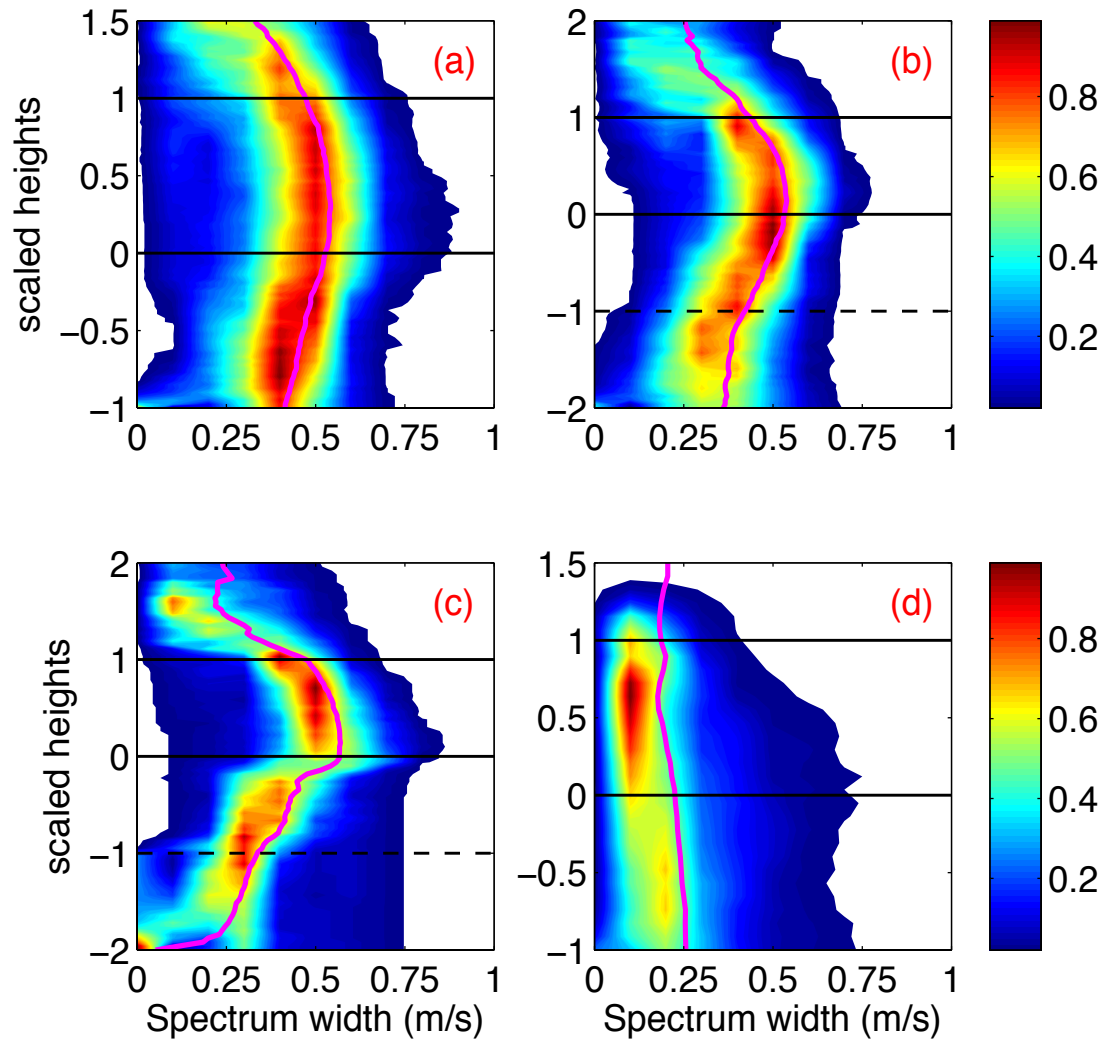
5 Figure 12: Same as Fig. 10 but for (a) clouds decoupled less than 450 m below cloud
 6 base and (b) clouds decoupled more than 500 m below cloud base.



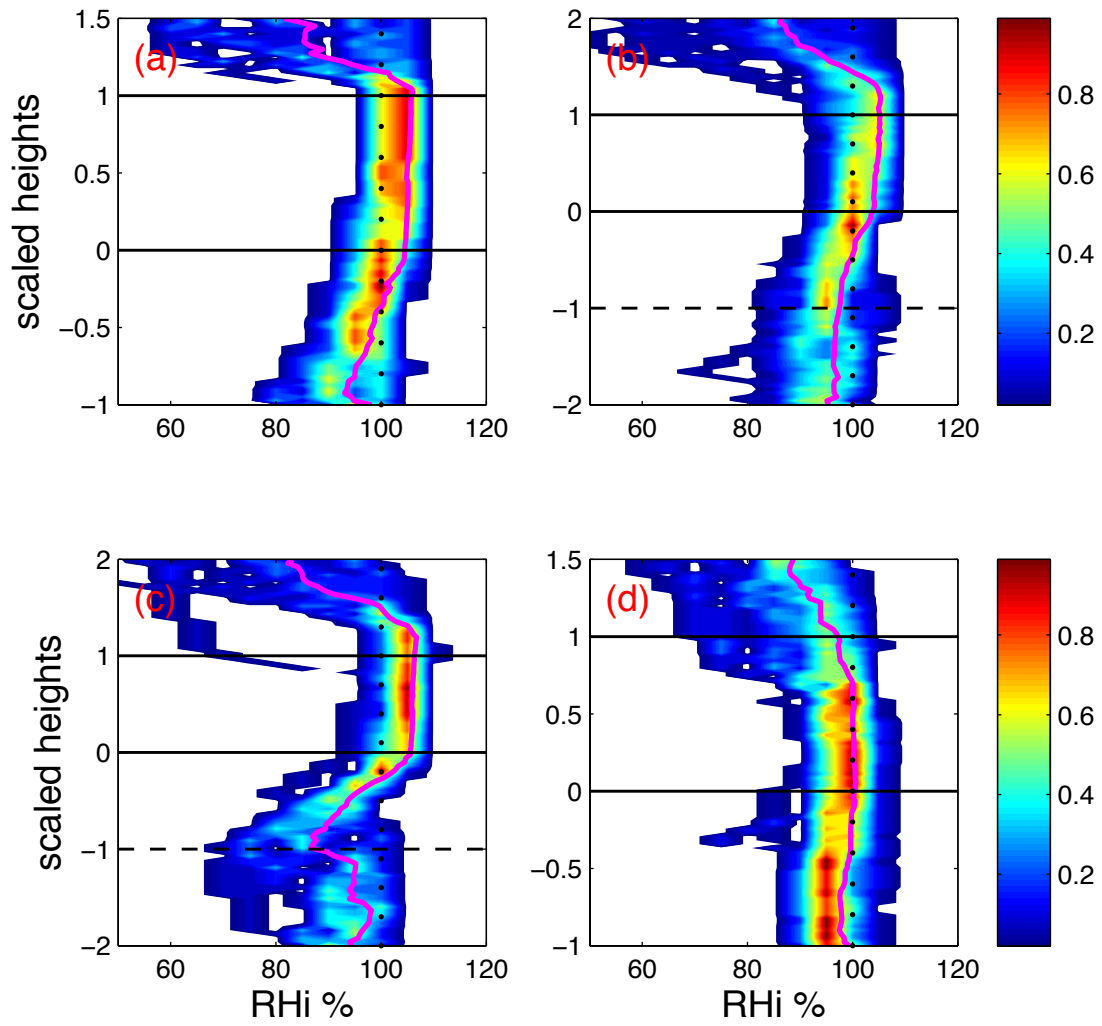
1 Figure 13: Box-and-whisker plots of scanning radiometer potential temperature
 2 gradient $d\Theta/dz$ [$^{\circ}\text{C m}^{-1}$] for (a) coupled, (b) weakly decoupled, (c) strongly
 3 decoupled and (d) stable clouds. The vertical scaling changes with cloud coupling
 4 state and is same as described in Fig. 10. Zero values are highlighted with dots.



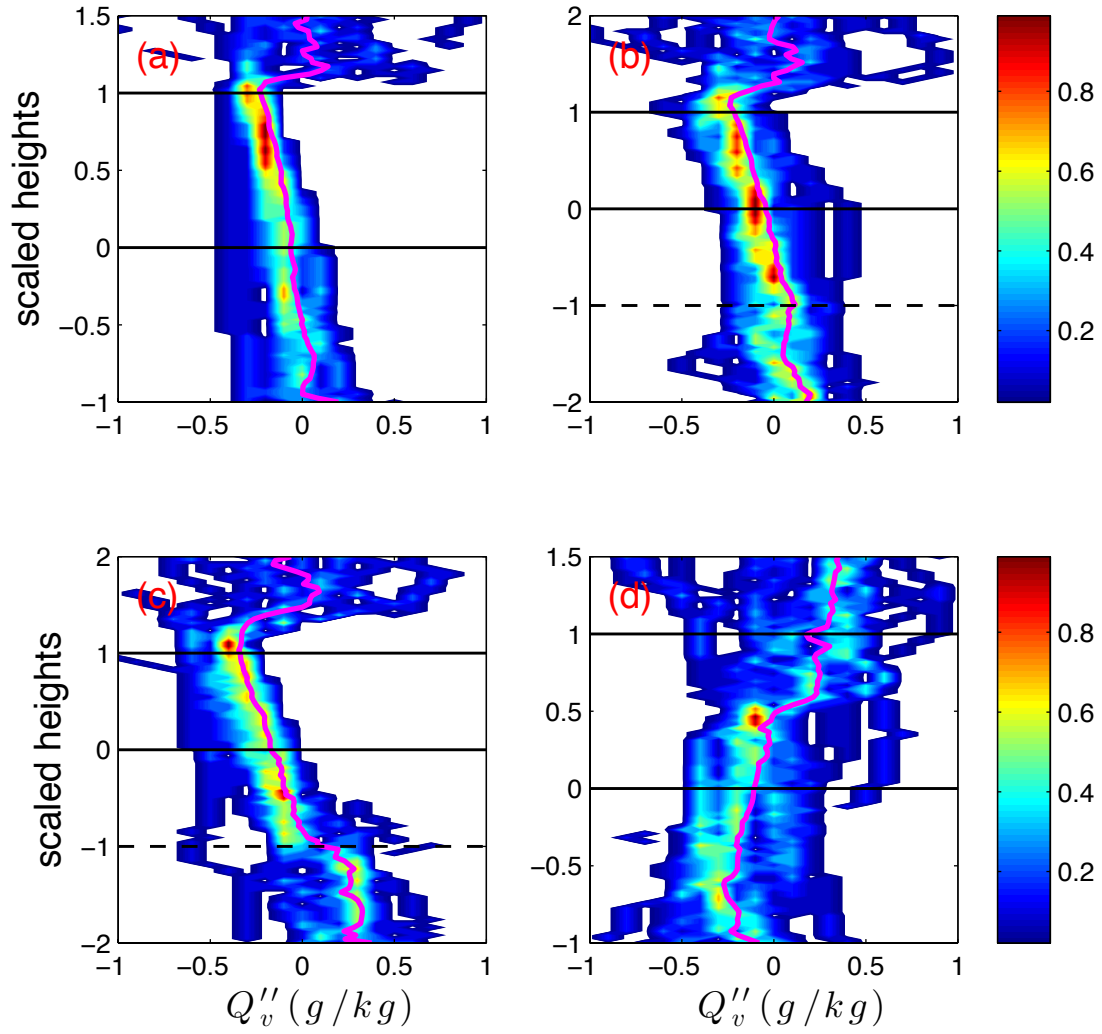
1 Figure 14: RFD contour plots of Doppler velocity [m s⁻¹] for (a) coupled, (b) weakly
 2 decoupled, (c) strongly decoupled and (d) stable clouds; magenta profiles are the
 3 medians. The vertical scaling changes with cloud coupling state and is same as
 4 described in Fig. 10. Zero values are highlighted with dots.



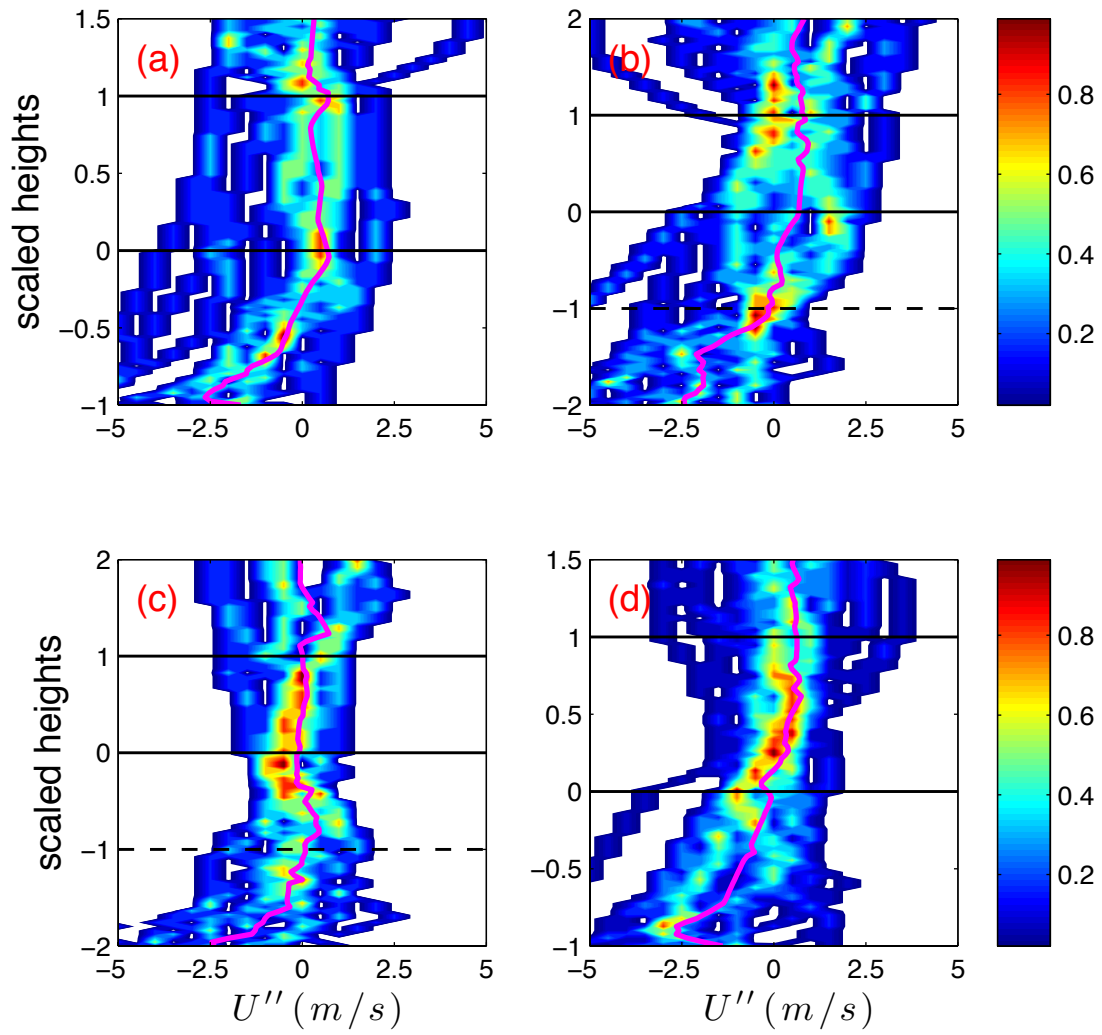
1 Figure 15: Same as Fig. 14, but for spectrum width [m s^{-1}].



1 Figure 16: Same as Fig. 14, but for radiosonde relative humidity [%] with respect to ice
 2 (RH_i). 100% values are highlighted with dots.



1 Figure 17: Same as Fig. 14, but for radiosonde scaled specific humidity [$g\ kg^{-1}$]. See
 2 section 3.5 for details on the scaling method.



1 Figure 18: Same as Fig. 14, but for radiosonde scaled wind speed [m s^{-1}]. See section 2 3.5 for details on the scaling method.